MITF-Independent Melanocyte Progenitors are Highly Susceptible to GNAQ-induced Uveal Melanoma in Adult Zebrafish

Julius I. Yevdash,[1] Rachel Moore,[1] Zhijie Li,[1] Katelyn R. Campbell-Hanson,[1] Delaney Robinson,[1] Danielle Gutelius,[3] Stephen P. G. Moore,[3] Dylan Friend,[1] Isaac O'Toole,[1] Robert A. Cornell,[2] Deborah Lang,[3] Ronald J. Weigel,[1,4] Colin Kenny[1,4,5]

1. Department of Surgery, College of Medicine, University of Iowa, Iowa City, IA 52242, USA.
2. Department of Oral Health Sciences, University of Washington, School of Dentistry, Seattle, WA, 98195
3. Department of Dermatology, Boston University School of Medicine, Boston, MA, 02118, USA.
4. Holden Comprehensive Cancer Center, University of Iowa, Iowa City, IA 52242, USA.
5. Lead Contact.

* Corresponding author: colin-kenny@uiowa.edu

Summary

Melanocytes reside in diverse microenvironments that influence their susceptibility to oncogenic transformation, however, studying rare melanoma subsets has been hindered by the lack of suitable animal models. We developed a primary, immune-competent zebrafish model to study uveal melanoma (UM), utilizing choroidal-targeted injection and electroporation of plasmids containing human *GNAQ*^{Q209L} and CRISPR/Cas9 cassettes for tumor suppressor gene deletion. Single-cell transcriptional profiling of genetically identical eye- and skin-derived tumors revealed distinct oncogenic pathways, highlighting the importance of studying melanoma subtypes in their correct anatomical context. Additionally, we identified a population of *tfec*- and *pax3a*-expressing melanocyte progenitor cells in *mitfa*-deficient embryos and adult zebrafish eyes, which were highly susceptible to GNAQ-driven transformation. While previous studies have linked *mitfa* deficiency to accelerated UM onset, our findings suggest that an expanded progenitor population in *mitfa*-deficient animals drives this susceptibility. Our study establishes a critical role for MITF-independent melanocyte progenitors in UM pathogenesis.

Highlights

- Choroid-targeted injection and electroporation of oncogenic *GNAQ* induces uveal melanoma in adult zebrafish.

- Germline loss of *mitfa* leads to expanded *mitfa*-independent melanocyte progenitor cells which are highly susceptible to GNAQ-driven transformation.

- Oncogenic BRAF and GNAQ transform molecularly and developmentally distinct subpopulations of cells within the melanocyte lineage.

Introduction

Uveal melanoma (UM) is a rare, poorly characterized cancer of the eye that has no effective FDA-approved therapeutic options for metastatic disease[1-3]. The majority of UM's (~90%) occur in the choroid, the vascular structure supplying the back of the eye, with the remainder arising from the ciliary body or the iris[4]. Choroidal UM's are considered slow-growing tumors that often remain asymptomatic and undetected until they reach a size that affects vision or are identified during a routine eye examination[5]. The absence of symptoms allows the tumor to persist undetected, providing time for the accumulation of genetic and epigenetic alterations that drive UM progression[6,7]. Distinguishing between non-cancerous, benign, and generally harmless choroidal nevi and early-stage UM remains a significant clinical challenge. The difficulty in obtaining biopsies of the choroid, coupled with the absence of anatomically accurate primary animal models, are key obstacles to understanding early-stage progression.

Targeted MAPK inhibitors and immune checkpoint inhibitors, the main therapies for cutaneous melanoma (CM), are not effective for the treatment of UM[8,9]. In addition to their differences in response to therapy, UM and CM display distinct metastatic progression. Up to 50% of UM's metastasize to the liver via hematogenous spread[3,10,11], whereas CM cells invade through the basement membrane and disseminate via the lymphatic system, resulting in a higher incidence of metastases to the bone, lungs, and the central nervous system (CNS), including brain[12-16]. The precise reasons for differential disease progression and response to therapy remain unclear; however, differences in their respective oncogenic drivers and the tumor microenvironment (TME) are likely to play a significant role in the distinct clinical features.

Oncogenic mutations in *GNAQ* or its paralog *GNA11* are observed in up to 90% of UMs[7] but are rare in CM. Such mutations reduce GTPase activity of the heterotrimeric G protein alpha

subunit, resulting in constitutive activation that drives cellular proliferation through downstream signaling pathways, including MAPK, YAP/TAZ, and PI3K signaling[4,17-19]. While *GNAQ/11* oncogenic mutations are uncommon in CM, the majority possess *BRAF* and *NRAS* mutations[4,20-22]. This distinction suggests that unique properties of melanocytes in different tissues, or perhaps their TME, may drive differential oncogene sensitivity. Melanocytes in the choroid interact with fibroblasts and vasculature endothelial cells, whereas melanocytes in the skin are in direct contact with keratinocytes. In transgenic experiments, $BRAF^{V600E}$-positive melanocytes exhibit significantly greater survival in the epidermis compared to $GNAQ^{Q209L}$-positive melanocytes. However, $GNAQ^{Q209L}$-positive melanocytes preferentially survive in the dermis, where fibroblasts are abundant[23]. This suggests that oncogene-specific interactions with the microenvironment influence melanocyte survival and provide a basis for the absence of GNAQ mutations in CM, except for dermal blue nevi which interact closely with fibroblasts. Interestingly, while UM and CM are unique in their metastatic patterns, GNAQ/11-mutant non-uveal melanoma demonstrates a lymphatic metastatic progression that resembles CM, thus further indicating the importance of studying UM in the correct anatomical context[21].

Zebrafish are a well-established model for studying melanocytes and melanoma due to conserved melanocyte differentiation pathways, efficient genetic manipulation, and the use of transparent lines that facilitate high-resolution live-cell imaging[21,24-32]. Zebrafish have three types of pigment cells; dark melanocytes, iridescent iridophores, and yellow xanthophores, that arise from multipotent, neural crest-derived pigment progenitors[21,30,33-36]. Melanomas have been shown to upregulate neural crest transcriptional programs, which are associated with worse clinical outcomes[26,37-39]. Similarly, *Tg(mitfa:GNAQ^{Q209L}); mitfa -/-* zebrafish, which retain melanocyte progenitor cells but lack differentiated melanocytes, have earlier occurrences of UM than wildtype counterparts[31]. By contrast, BRAF-driven CM displays a reliance on Mitfa activity to progress[40,41]. To study the early events of UM, we developed a novel zebrafish model that

utilizes the transgene electroporation of adult zebrafish (TEAZ) approach to express the human GNAQ^{Q209L} oncogene in cells of the melanocyte lineage within the skin and eye. By targeting injections to the choroid, primary UM tumors arise from the same anatomical location as human UM, recapitulating similar TME and initiating cell types. In this study, we analyze expression differences between genetically identical skin and eye-derived GNAQ^{Q209L} tumors and demonstrate the existence of a melanocyte precursor population in the eyes of *mitfa* -/- zebrafish that have an increased sensitivity to transformation by GNAQ^{Q209L}.

Results

Generation of plasmid constructs to drive GNAQ^{Q209L}-induced melanoma.

To study GNAQ-driven melanoma in adult zebrafish, we generated expression plasmids containing two cassettes under the control of the *mitfa* promoter. The first cassette encoded human oncogenic *GNAQ^{Q209L}* fused to a T2A self-cleaving peptide followed by eGFP, while the second cassette expressed CRISPR/Cas9. Additionally, three zebrafish U6 promoters were used to drive gRNAs targeting *tp53* and *ptena/b* (**Figure 1A** – strategy A). Recognizing that T2A cleavage results in residual amino acids remaining on the C-terminus of GNAQ, which may alter its oncogenic activity, we employed an alternative delivery strategy. This system utilized five separate plasmids: (1) *mitfa:GNAQ^{Q209L}; mitfa:eGFP* (a generous gift from Dr. Jacqueline Lees at the KOCH institute Massachusetts Institute of Technology), (2) *mitfa:Cas9*, (3) *U6:*gRNA-*tp53*, (4) *U6:*gRNA-*ptena* and (5) *U6:*gRNA-*ptenb* (**Figure 1A** – strategy B) (plasmids 2-5 were a generous gift from Dr. Richard White at the University of Oxford, UK). This design aimed to improve the oncogenicity of GNAQ^{Q209L} by avoiding unintended C-terminal modifications by T2A cleavage. Moreover, the plasmids used in strategy B are smaller in size, which may enhance the efficiency of uptake during electroporation.

We applied TEAZ to the skin (TEAZ-Skin) of adult wild-type (AB), *mitfa*$^{w2/w2}$ (nacre[42]), and *mitfa*$^{w2/w2}$*; mpv17*$^{a9/a9}$ (casper[43,44]) zebrafish to validate the oncogenic potential of *GNAQ*^{Q209L} (**Figure 1B**). TEAZ-Skin using Strategy A and Strategy B induced melanoma in wild-type zebrafish within 160 and 100 days, respectively (**Figure 1C-D**). TEAZ-Skin with only a subset of the Strategy B plasmids such as oncogenic GNAQ alone or only Cas9-mediated tumor suppressor deletions did not induce melanoma, suggesting that both oncogenic GNAQ and tumor suppressor deletion are required for transformation (**Figure 1D**).

TEAZ-Skin was subsequently applied to zebrafish lacking functional *mitfa* (nacre and casper lines), which lack differentiated melanocytes. Consistent with previous observations in transgenic *Tg(mitfa-GNAQ*^{Q209L}*); mitfa*$^{w2/w2}$*; tp53*$^{-/-}$ zebrafish[31], *mitfa* loss resulted in decreased tumor latency compared to wild-type zebrafish (**Figure 1E-H**). Tumors were detected within 70- and 40-days post-electroporation following Strategy A and Strategy B, respectively. Moreover, unlike wild-type zebrafish, expression of oncogenic GNAQ alone was sufficient to induce melanoma in casper (*mitfa*$^{w2/w2}$ *: mpv17*$^{a9/a9}$) and nacre (*mitfa*$^{w2/w2}$) (**Figure 1I-J**). In contrast, human oncogenic *BRAF* failed to induce melanoma in *mitfa*-deficient animals, by TEAZ-Skin, unless *mitfa* was re-expressed, as previously reported[26,31]. Together, our findings demonstrate that both TEAZ-Skin strategies are sufficient to induce GNAQ-driven melanoma, with strategy B demonstrating reduced tumor latency. Notably, TEAZ-Skin accelerates melanoma onset relative to transgenic models; while tumors in transgenic *Tg(mitfa:GNAQ*^{Q209L}*)* zebrafish typically arise 200-400 days post-fertilization[31], TEAZ-Skin induces UM tumors by approximately 100 days.

The *mitfa*-promoter is active in choroidal melanocytes.

Having confirmed the oncogenicity of our *GNAQ*^{Q209L} expression plasmids using TEAZ-Skin, we next sought to adapt this approach to induce melanocyte transformation in the zebrafish eye (TEAZ-Eye), specifically targeting the choroid, where the majority of ocular melanocytes reside (**Figure 2A-B**). To determine whether TEAZ-Eye could serve as a model for UM in adult zebrafish, we first assessed the specificity of the *mitfa* promoter in driving transgene expression in choroidal melanocytes. To this end, we harvested eyes from transgenic *Tg(mitfa:GFP)* zebrafish and performed immunofluorescent imaging using an anti-GFP antibody. Choroidal melanocytes exhibited strong anti-GFP positivity compared to the secondary-only control (**Figure 2C-D**). Of note, the retinal pigment epithelium (RPE), located apically to the choroidal melanocytes, contains autofluorescent granules. Quenching the autofluorescence signal from the RPE improved the anti-GFP signal-to-noise ratio (**Figure S1A**). We next applied TEAZ-Eye (**Figure 2E)** by injecting and electroporating plasmids containing the *mitfa* promoter driving *eGFP* expression (*mitfa:eGFP*) into the choroid. Eyes were harvested two weeks post-electroporation, and immunofluorescence using an anti-GFP antibody was performed. Remarkably, cells at the injection site exhibited a strong eGFP signal compared to the secondary-only control (**Figure S1B**). These results demonstrate that the *mitfa* promoter is sufficient to drive transgene expression in choroidal melanocytes.

TEAZ-Eye induces UM in the choroid of wild-type and casper zebrafish

A major limitation in the study of UM onset and progression is the lack of anatomically accurate *in vivo* models. For instance, UM tumors derived in transgenic *Tg(GNAQ*^{Q209L}*): tp53*$^{-/-}$ zebrafish predominantly form in the skin, with ~1-2% of tumors forming in the eye[31]. To address this gap, we applied TEAZ-Eye using a plasmid pool containing *mitfa:GNAQ*^{Q209L}*, mitfa:Cas9, U6:*gRNA-*tp53, U6:*gRNA-*ptena, and U6:*gRNA-*ptenb* (i.e., Strategy B) into the choroidal space of wild-type zebrafish, followed by electroporation (**Figure 2E**). Remarkably, TEAZ-Eye in wild-type

zebrafish resulted in the transformation of cells within the choroid. Live *in vivo* imaging of TEAZ-Eye enabled the identification of single GFP+ cells at the injection site, serving as a proxy for *GNAQ*^{Q209L} expression (**Figure 2F-K, 2F'-K'**). Similar to human UM, TEAZ-Eye UM progressed slowly, leading to nodular tumors between 42-92 days post electroporation. We next applied TEAZ-Eye to *mitfa*-deficient casper zebrafish, and, like TEAZ-Skin, large tumors developed within 21 days post-electroporation (dpe) (**Figure 2L-N, 2L'-N'**). H&E analysis confirmed that TEAZ-Eye induced UM within the choroid, progressing into surrounding ocular structures (**Figure 2O**). Notably, 100% (n=10 tumors) of tumors formed between the sclera and RPE, highlighting the model's ability to induce anatomically accurate UM. Finally, immunofluorescent analysis using anti-GFP antibodies confirmed the expression of plasmid constructs following TEAZ-Eye (**Figure 2P-Q**).

UM transformation involves activation of neural crest transcriptional programs

During embryonic development, choroidal melanocytes are derived from the cranial neural crest (CNC). Since our model can detect the earliest events in UM transformation, we asked whether the reactivation of CNC programs is one of the initial steps in UM development. To achieve this goal, tumors were derived in wild-type zebrafish using TEAZ-Eye with Strategy B plasmids. At 50 dpe, when gross nodular tumors were identified (**Figure 3A**), surgical enucleation was performed, and dissociated cells from the entire eye were analyzed using single-cell RNA sequencing (scRNA-seq) (**Figure 3B**). Tumor cells were identified by expression of *GFP* (**Figure 3C**) whereas annotation of cell types within the tumor microenvironment (TME) was accomplished by comparing to previously published scRNA-Seq datasets using human choroid and retina[45,46], the Zebrafish Information Network (ZFIN)[47], and from the zebrafish embryo single cell atlas "Daniocell" (**Figure 3D**). Immune cell populations within the TME included B-cells (*igic1s1, pax5, cd79a, zgc:153659*), T-cells (*traf1, si:ch211-67e16.3, cd27, zap70, cd8a, sla2*), a

population of cytokine producing cells, likely representing T-Cells (*il4, il13, il11, ca2, il34, il6*) as well as macrophages (*marco, ccl34a.4, mrc1b, c1qa/b/c, grn1*) and neutrophils (*cpa5, lect2l, mmp9, npsn, scpp8*). Additional cell types within the choroidal TME included fibroblasts (*col1a1a, col1a1b, col1a2, col5a1, dcn, serpinf1*) and vasculature endothelial cells (*vwf, epas1b, ecscr, fabp11a*). Profiling GFP+ UM cells revealed that UM tumors exhibited strong expression of neural crest markers (*tfap2a, tfap2c, pax7b, sox10, foxd3*) and melanocytic markers (*mitfa, tfap2e, mlana, pmela, tyrp1a, pgfa, mtbl*). CNC marker genes *twist1* or *dlx1* were not enriched in UM tumors compared to the TME. Our results demonstrate that GNAQ-induced transformation of choroidal melanocytic cells occurs either through the activation of neural crest transcriptional programs or through the transformation of a cell with pre-existing neural crest gene signatures that persist in UM tumors. (**Figure 3D)**

GNAQ-driven tumors are influenced by their TME

The eye TME is distinct from that of the skin, and our model provides a unique opportunity to characterize the degree to which the TME influences transcriptional programs within tumor cells. To this end we generated genetically identical tumors using TEAZ-Eye and TEAZ-Skin with strategy B plasmids in wild-type zebrafish (**Figure 3A and Figure 3E**) and performed scRNA-seq. UMAP analysis revealed distinct clustering of eye-derived (red) and skin-derived (blue) tumors (**Figure 3F-G, Figure S2A-C**). To identify the transcriptional differences between tumors derived from TEAZ-Eye and TEAZ-Skin based on the TME, we compared the gene expression profiles of each tumor type relative to its respective TME. In total, 4,627 genes were enriched in TEAZ-Skin tumors, and 3,283 genes were enriched in TEAZ-Eye tumors (**Table S1**). Of these, 2,782 were uniquely enriched in TEAZ-Skin, 1,438 were uniquely enriched in TEAZ-Eye, and 1,845 were shared (**Figure 3G'**). Pathway analysis showed that the genes enriched in TEAZ-Eye-derived tumors were associated with NF-kB, RHO GTPase, and NOTCH activity, as well as

RAF/MAP kinase, mTOR, and PI3K/AKT signaling (**Figure S3-S4**). Analysis of TEAZ-Skin-enriched genes revealed the Neddylation pathway, RHO GTPase and regulation of mitotic cell cycle checkpoints and DNA synthesis (**Figure S5**). Moreover, differential expression analysis between eye and skin tumors identified several genes that are uniquely upregulated in eye tumors, including lectin, galactoside-binding, soluble, 2 (*lgals2a*), fatty acid binding protein 3 (*fabp3*) and the proto-oncogene, receptor tyrosine kinase (*kita*) (**Figure 3H**). Interestingly, relatively high expression of fatty acid-binding proteins *FABP3, FABP5,* and *KIT* are predictive of worse overall survival (OS) in UM and, to a lesser extent, in CM patients (**Figure S6**). Notably, these genes are also associated with worse disease-free survival (DFS) in UM, while their expression does not correlate with DFS in CM (**Figure 3I**). Similarly, high expression of *LGALS2* is strongly associated with worse OS in UM, however, in CM elevated *LGALS2* expression is linked to improved OS, based on TCGA datasets (**Figure 3H–J**). These results highlight the role of the TME in UM pathogenesis; however, the observed signaling differences may also reflect contributions from distinct cells-of-origin between skin and eye melanocyte populations. Together, our findings demonstrate the utility of our model to identify candidate genes involved in human UM pathogenesis.

Melanocyte progenitor cells are highly susceptible to oncogenic GNAQ transformation in *mitfa*-deficient zebrafish.

Given that loss of *mitfa* in adult zebrafish accelerates UM onset, we asked whether similar effects would be observed in the eye, and whether the loss of *mitfa* affected the cell of origin of UM in *mitfa*-deficient zebrafish. We first compared UM onset following TEAZ-Eye in wild-type (n=5), nacre (n=3), and casper (n=6) zebrafish and found that tumor latency and progression were significantly reduced in *mitfa*-deficient lines (**Figure 4A**), thus recapitulating our observations using TEAZ-Skin (**Figure 1J**). H&E analysis of nacre zebrafish eyes showed loss

of choroidal melanocytes (**Figure 4B**), whereas melanin in the RPE remains less affected, as previously shown[30]. These observations imply that an *mitfa*-independent melanocyte progenitor cell persists in nacre and casper zebrafish and that they are susceptible to oncogenic GNAQ transformation. To identify such cells, we crossed *mitfa*$^{w2/w2}$ with *Tg(mitfa:GFP)* lines to create *Tg(mitfa:GFP); mitfa*$^{w2/w2}$ zebrafish. We then harvested adult eyes at 5 months and performed anti-GFP immunofluorescence analysis. While GFP+ melanocytes were readily detected in the choroid of *Tg(mitfa:GFP)* zebrafish (**Figure 2C-D**), staining of *Tg(mitfa:GFP); mitfa*$^{w2/w2}$ eyes revealed rare cells with GFP-positivity (**Figure 4C**). Such GFP+ cells were primarily located in the ciliary body, with isolated cells also found in the choroid, suggesting the persistence of a *mitfa*-independent progenitor population in adult *mitfa*-deficient zebrafish (**Figure 4C**). We next asked whether such cells retain the ability to undergo melanocyte differentiation by using TEAZ-Eye to deliver plasmids containing the *mitfa*-promoter driving expression of *mitfa* (i.e., to overexpress *mitfa* mRNA expression). Interestingly, overexpression of *mitfa* transcript levels resulted in expansion of choroidal melanocytes in wild-type animals and the rescue of choroidal melanocytes in *mitfa*-deficient (nacre) zebrafish as shown by H&E analysis (**Figure S7A-B'**). To assess whether GFP-positive cells are sensitive to oncogenic transformation by GNAQ, we expressed *mitfa-GNAQ*^{Q209L} in *Tg(mitfa:GFP); mitfa*$^{w2/w2}$ zebrafish using TEAZ-Eye. In all injected fish (n=3), UM tumors were GFP-positive, suggesting they originated from GFP+ progenitor cells within the eye of *Tg(mitfa:GFP); mitfa*$^{w2/w2}$ zebrafish (**Figure S7C**).

Melanocyte progenitor cells express neural crest marker genes in *mitfa*-deficient zebrafish.

We performed scRNA-Seq and pseudotime analysis on UM tumors from the eyes of *mitfa*-deficient (casper) zebrafish and compared them to normal casper eye tissue. Within the casper eyes, we identified a population of cells expressing the *nacre* allele that clustered closely with

UM tumors under TEAZ-Eye conditions, termed progenitors (**Figure 4D, Figure S8A-B**). We re-clustered the progenitor and tumor cells (**Figure 4E**), revealing seven distinct clusters consisting of neural crest like (NC-like), melanoblast-like, proliferating, progenitor, angiogenic, stress-like, as well as an unidentified cluster marked by *tmsb1, krt91* and *vim* (**Figure 4E, 4G**). Pseudotime analysis supports a lineage trajectory from the progenitor cells to heterogeneous UM tumor cells (**Figure S8C**). Notably, the progenitor cell population in normal casper eyes expressed neural crest and melanocyte stem cell marker genes, including *tfap2a, foxd3, sox10*, *pax3a, vim,* and *yap1* (**Figure 4F-G**). UM tumor cells retained expression of these genes but activated additional genes associated with pigment progenitor cell function, including *tfec* and *kita* (**Figure 4G**). Interestingly, despite the lack of Mitfa activity in casper zebrafish, GNAQ-positive UM tumors included a melanoblast-like cluster that exhibited expression of pigmentation genes, including *pmela, mlpha*, and *mlana,* likely explaining the occasional emergence of melanin within tumors as they progress in casper zebrafish.

mitfa-deficient zebrafish exhibit expanded _pax3a_ and _tfec_ positive melanocyte progenitors during embryogenesis.

Having established that an Mitfa-independent progenitor population gives rise to UM in *mitfa*-deficient zebrafish, we next examined whether this population is expanded relative to wild-type zebrafish. To test this prediction, we performed scRNA-seq on GFP-positive cells sorted from *Tg(mitfa:GFP)* and *Tg(mitfa:GFP);mitfa*$^{w2/w2}$ transgenic zebrafish embryos at 28 hours post fertilization (hpf), when melanocytes (zebrafish melanophores) begin to differentiate. We assigned cell-type annotations based on our previously annotated GFP-positive cells from *Tg(mitfa:GFP)* embryos[27]. The 10 clusters included six main cell types: neural crest cells (*sox10, foxd3*), a tripotent precursor of melanoblasts (M), iridoblasts (I), and xanthoblasts (X) (*tfap2a*, *cdkn1ca, slc15a2, ino80e, id3, mycn, tfec*), termed MIX cells, a cluster that expressed high

levels of melanoblast/xanthoblast markers (*mitfa, erbb3b, impdh1b, gch2, id3*), termed MX cells, a melanoblast cluster (*mitfa, dct, pmel, tyr*), as well as two additional clusters corresponding to xanthoblasts and xanthophores. For this analysis we referred to MIX and MX cells as melanophore progenitors (**Figure 4H**). As expected, melanophore cells were reduced in *Tg(mitfa:GFP): mitfa*$^{w2/w2}$ zebrafish (**Figure 4H-I**). However, melanophore progenitors were expanded in *Tg(mitfa:GFP);mitfa*$^{w2/w2}$, while neural crest cells remained unaffected (**Figure 4I**). Melanophore markers were downregulated in GFP-positive cells sorted from *Tg(mitfa:GFP);mitfa*$^{w2/w2}$*,* whereas melanocyte progenitor markers (*pax3a, sox10, foxd3*), as we identified in adult zebrafish eyes (**Figure 4F**), were upregulated in embryonic progenitors from *Tg(mitfa:GFP);mitfa*$^{w2/w2}$ embryos (**Figure 4J**). A role for *pax3a* in adult fish eye tissue was not characterized prior. In parallel, a *pax3* expressing population was identified in adult C57BL/6 mouse eyes in the limbal region, and rarely in the choroid (**Figure S9**). These findings support a rare pax3-expressing population in both fish and mice eyes, and may mirror pax3 expression in the melanocyte stem cell in the skin.

Conditional deletion of *mitfa* in adult zebrafish fails to recapitulate germline loss-of-function effects on tumor-free survival in GNAQ-driven melanoma.

We next investigated whether the accelerated growth of GNAQ-driven tumors in casper and nacre zebrafish, compared to wild-type animals, was due to an expansion of progenitor cells or the cell-intrinsic loss of Mitfa activity. To this end, we performed conditional *mitfa* knockout experiments using Strategy B plasmids in combination with either (1) non-targeting control gRNAs or (2) gRNAs targeting exon 5 of mitfa. TEAZ-Skin was performed in three experimental groups: (1) casper zebrafish (n=6) with gRNAs targeting *mitfa* (which cuts after the *nacre* allele and serves as an off-target control), (2) wild-type zebrafish (n=6) with non-targeting gRNAs, and (3) wild-type zebrafish (n=6) with U6-gRNA-mitfa. Of the injected zebrafish, 6 of 6 *casper*, 1 of 6

wild-type (+U6-mitfa), and 0 of 6 wild-type (+non-targeting) zebrafish developed tumors within 60 days post-electroporation (dpe) (**Figure 4K**). Interestingly, the single amelanotic tumor that formed following conditional deletion of *mitfa* in a wild-type zebrafish developed at 32 days, which is similar to tumor onset in casper. Such observations suggest that the loss of *mitfa* from differentiated melanocytes may create a vulnerable transcriptome for GNAQ-induced transformation. Alternatively, this tumor may have resulted from a transformed melanocyte progenitor cell that, in the absence of *mitfa*, failed to differentiate, contributing to tumor onset. Of note, tumors that formed in *mitfa*-deficient zebrafish developed distal metastases, an observation not seen in *mitfa* wild-type TEAZ-Skin injected zebrafish (**Figure 4K', Figure S10**). Our findings support a model in which failed differentiation as well as the expansion of melanocyte progenitor cells in *mitfa*-deficient animals creates a permissive cellular environment for GNAQ-induced transformation and reduced tumor latency.

Transcriptional programs enriched in BRAF- versus GNAQ-driven melanoma overlap with specific melanocyte progenitor populations.

Oncogenic BRAF and NRAS are unable to promote transformation in the absence of *mitfa*[26,29], suggesting that distinct transcriptional programs, potentially reflecting unique cellular origins, are required for UM and CM transformation. To address this hypothesis, we analyzed previously published scRNA-seq datasets in transgenic *Tg(mitfa:BRAF^{v600e}): tp53$^{-/-}$* : *mitfa$^{w2/w2}$* zebrafish where TEAZ-Skin was used to rescue *mitfa* and induce melanoma[29], to our GNAQ-induced tumors by TEAZ-Skin (**Figure 5A)**. We predicted that by analyzing primary tumors, the transcriptional signature of the origin cell will be retained and can be identified by overlapping gene signatures identified in the embryonic melanocyte lineage[27]. Interestingly, while the expression of *mitfa* was significantly higher in GNAQ-positive tumors (Log2FC > 4, FDR < 0.0001), the expression of pigmentation genes; including *trpm1b, tyrp1b* and *pmela* were

significantly higher in BRAF-positive melanoma, while *mlana* was higher in GNAQ-positive tumors (**Figure S11**). Genes enriched in UM and CM were identified by those with a Log2FC > 1 and FDR < 0.05 between the two tumor types (**Figure 5B**). We next overlapped this differential gene signature with genes expressed by cells within the melanocyte lineage isolated from zebrafish embryos (**Figure 5C**). As expected, BRAF-driven tumors strongly mapped to the melanoblast and melanophore clusters (**Figure 5D**), supporting recent findings that BRAF-driven melanoma originates from melanoblasts, a melanocyte progenitor population[29,48]. When comparing GNAQ-enriched genes to the melanocyte lineage, we found that the signatures were not confined to a single cluster but were distributed among neural crest cells, melanocyte progenitors, and xanthophore clusters (**Figure 5D; Figure S12**). Such results support the hypothesis that GNAQ- and BRAF-driven melanomas depend on distinct transcriptional programs, reflecting less and more differentiated melanocytic states, respectively.

Discussion

Herein, we present a highly penetrant, immunocompetent zebrafish model of primary UM where tumors arise within the choroid and progressively invade surrounding ocular structures. This model enables the study of the earliest events of UM pathogenesis and how anatomical context impacts disease progression. Notably, genes identified through our analysis correlate with survival differences in human UM, highlighting the model's potential for mechanistic studies on gene function in UM pathogenesis. Compared to transgenic models, our system produces anatomically correct tumors at an accelerated rate, offering an efficient platform for studying UM progression and therapeutic responses.

Although UM and CM both arise from cells within the melanocyte lineage, they differ significantly in their biology and clinical outcomes. To explore how anatomical context influences

transcriptional states, we compared genetically identical tumors derived in the skin and eye and found that eye-derived tumors display distinct expression profiles. Specifically, we found that fatty acid binding proteins, particularly *fabp3*, are enriched in UM tumors arising in the eye compared to those in the skin. While lipid droplets have been identified as vulnerable targets in CM and regulators of melanoma plasticity[29,49], lipid signaling in UM has received limited attention[50-53]. Interestingly, high expression of *FABP3* as well as *FABP5* associates with worse disease-free survival in patients with UM but not in CM. Additionally, we observed elevated Rho/Rac and MAPK signaling in UM tumors derived by TEAZ-Eye. Rho/Rac signaling has been characterized as a key pathway in UM pathogenesis through its regulation of YAP activity and actin polymerization[54]. Interestingly, while our model demonstrates upregulation of genes in the MAPK pathway in UM compared to CM, the role of MAPK signaling in UM remains less well defined. One study reported that MAPK activity varies across primary UM samples[55], and another study using transgenic UM zebrafish reported that ERK1/2-MAPK activation is unlikely to be a major player in UM pathogenesis[56]. Such observations imply that MAPK activity may contribute to UM onset but is not necessary for its progression. Finally, we found greater *kita* expression in GNAQ-driven tumors in the eye compared to those in the skin, a result that is particularly notable given recent studies linking KIT-positive tumors with poor prognosis and monosomy of chromosome 3[57]. Using our animal model to compare genetically identical tumors across different anatomical sites has revealed distinct biological behaviors, highlighting the model's potential for further investigations into site-specific tumor biology and therapeutic strategies.

An interesting distinction between GNAQ and BRAF oncogenes is their differential dependency on Mitfa activity for tumorigenesis. While $BRAF^{V600E}$ requires Mitfa activity to induce melanoma[24,26], $GNAQ^{Q209L}$-driven tumor latency was significantly reduced in *mitfa*-deficient zebrafish compared to wild-type controls. Our results are consistent with prior studies showing

that *mitfa*-deficient zebrafish activate distinct signaling pathways, favoring YAP over MAPK signaling, and give rise to tumors with accelerated growth compared to wild type tumors. Moreover, manipulating YAP activity in wild-type animals was shown to recapitulate the enhanced growth seen in *mitfa*-deficient tumors[37]. We observed high *yap1* expression in melanocyte progenitor cells of *mitfa*-deficient zebrafish, suggesting that elevated YAP activity may be carried over from the progenitor cell during transformation. While *mitfa* loss accelerates tumor onset, our data suggest this is not due to the deletion of *mitfa* from differentiated melanocytes. Instead, we propose that *mitfa* deficiency expands a pool of *pax3a*- and *tfec*-positive melanocyte progenitor cells, which may be more susceptible to transformation. Interestingly, these progenitor cells appear to maintain a neural crest signature, as evidenced by the relatively high expression of additional markers such as *foxd3, sox10,* and *tfap2a*. Supporting this notion, melanocyte-specific conditional knockout of *mitfa* in wild-type zebrafish did not result in reduced tumor latency compared to non-targeting controls. Together, these findings suggest that germline loss of *mitfa*, rather than its conditional deletion, enhances the transformation potential of melanocyte progenitor cells by expanding them and maintaining a neural crest-like transcriptional profile.

Studies in human UM have shown that less pigmented tumor regions are more metastatic and that BAP1-negative tumors exhibit a stem-like phenotype[1,2,58,59]. Our findings raise intriguing questions about whether the progenitor cells observed in *mitfa*-deficient zebrafish are similarly predisposed to a more undifferentiated, stem-like phenotype, contributing to their enhanced transformation potential and aggressive tumor behavior. Furthermore, differences in *mitfa* dependency between BRAF-driven cutaneous melanoma and GNAQ-driven UM suggest fundamental distinctions in their cellular origins. Although MITF-independent melanocytic cells are unlikely to be the cellular origin of CM in zebrafish models, studies have shown that MITF-independent BRAF-positive melanoma cells are central to disease recurrence[41].

While BRAF-driven transformation in zebrafish depends on Mitfa activity, GNAQ-driven transformation may be facilitated by Mitfa paralogs such as Tfec and Tfeb. The Mitfa paralog Tfec has been shown to activate pigmentation genes in both the retinal pigment epithelium and melanocyte progenitor cells. Tfec can also rescue ectopic melanocytes in *nacre* zebrafish embryos[28,30]. Moreover, we have recently shown that the MITF paralog TFE3 promotes cellular plasticity and stemness genes in MITF-low melanoma cells[60], suggesting that MITF paralogs are compelling candidate transcription factors in UM pathogenesis.

Beyond melanocytes, we must also consider the broader cellular environment in UM. The global loss of *mitfa* could have secondary effects on other cell types, such as immune cells, which may influence tumor behavior. The presence of xanthophore, iridophore, and melanophore markers within UM tumor cells raises the possibility of a pluripotent progenitor population. This model also enables us to examine whether differences in differentiation potential contribute to tumor aggressiveness, as casper fish may exhibit more pronounced tumor acceleration due to the simultaneous blockade of two chromatophore differentiation pathways compared to single-pathway inhibition in nacre fish.

Our findings open numerous avenues for future research. This model can be used to study the effects of *BAP1* loss and other secondary mutations commonly associated with UM, such as *EIF1AX* and *SF3B1*. It also provides a platform for investigating metastatic events, as tumors emerge in defined primary sites. Establishing zebrafish UM cell lines from different anatomical locations and genetic backgrounds could offer further insights into the role of microenvironment and *mitfa* dependency in UM progression. Additionally, characterizing the melanocyte progenitor population in the eye and determining if a similar population exists in mammals could provide critical insights into uveal stem cell biology. While we identified a population of Pax3-positive

cells in the mouse limbus, it remains to be determined if these cells are sensitive to oncogenic GNAQ transformation.

Limitation of study

The use of *tp53* and *ptena/b* mutations in our UM model does not fully recapitulate the genetics of human UM. Mutations in *TP53* and *PTEN* are rarely observed in this cancer, where loss-of-function mutations in *BAP1* represent the most frequent tumor suppressor alteration[61-63]. However, both *TP53* and *PTEN* signaling pathways have been shown to be altered in UM pathogenesis. MDM2 overexpression, an upstream negative regulator of p53, and downregulation of PERP, a downstream effector of p53, have been demonstrated in many UM patients and are associated with worse outcome[64-68]. Studies have also shown that over half of UM tumors have decreased PTEN immunostaining and its loss is correlated with decreased survival[62,69,70]. Nevertheless, whether genetic knockout of these tumor suppressors recapitulate the dysregulation of these pathways in human UM remains an open question. Another limitation to our approach when examining the differences between genetically identical skin and eye-derived tumors is the inability to distinguish between purely microenvironmental effects and differences in cell of origin (melanocytes in the skin versus in the eye). To address this question, a syngeneic or immunodeficient model could be applied to transplant cells from a primary UM tumor into both anatomical sites. Additionally, our use of the *mitfa* promoter to drive oncogene expression presents a challenge in defining the exact cell of origin, as this promoter is active in both melanocyte progenitors and differentiated melanocytes. As such, it remains unclear whether tumors in *mitfa* wild-type fish (or those with conditional *mitfa* deletion) arise from a progenitor or a mature melanocyte. Lineage tracing studies will be essential to determine

whether differentiated melanocytes possess the capacity to initiate primary UM in *mitfa*-competent or conditional *mitfa*-KO zebrafish.

Resource availability

Lead contact

Requests for further information and resources should be directed to, and will be fulfilled by, the lead contact, Colin Kenny, PhD (colin-kenny@uiowa.edu).

Materials availability

Plasmid constructs and zebrafish generated in this study may be obtained by a request to the lead contact.

Data and code availability

Datasets generated in this article are available from NCBI GEO accession number GEO: Pending. This study does not report original code. Any additional information required to reanalyze the data reported in this work paper is available from the lead contact upon request.

Acknowledgments

This project was supported by grants from the Holden Comprehensive Cancer Center (HCCC; P30- CA086862) at the University of Iowa. Additional support came from an institutional research grant from the American Cancer Society, administered through the HCCC, to C.K. (IRG-18-164-43) and from the Melanoma Research Alliance (ID#1426690) to C.K. Additional support came from the National Institutes of Health (NIH) to R.A.C. (R01-AR062457). The funders had no role in study design, data collection and analysis, decision to publish, or

preparation of the manuscript. We gratefully acknowledge Dr. Richard White from Oxford University, UK. for providing mitfa-Cas9, *U6*:gRNA-*ptena*, *U6*:gRNA-*ptenb* and *U6*:gRNA-*tp53* plasmids constructs and for providing critical comments to successfully preform TEAZ experiments. We additional acknowledge Dr. Jacqueline Lees and Mr. Adam Amsterdam from the Koch Institute for Integrative Cancer Research at MIT for generously providing *mitfa*:*GNAQ*^{Q209L}; *mitfa*:GFP plasmid constructs to induce UM tumors.

Author contributions

Conceptualization: C.K. Methodology: J.I.Y., R.M., Z.L., K.R.C-H., D.R., D.G., S.P.G.M., D.F., I.O.T. Investigation/data analysis: J.I.Y., R.M., Z.L., K.R.C-H., D.R., D.G., S.P.G.M., D.F., I.O.T. C.K. Visualization and data interpretation: J.I.Y., R.M., Z.L., K.R.C-H., D.R., D.G., S.P.G.M., D.F., I.O.T. D.L., R.J.W., and C.K. Funding acquisition: R.A.C., D.L., and C.K. Project administration: C.K. Supervision: C.K. Writing—original draft: J.I.Y., and C.K. Writing—review and editing: J.I.Y., D.L., R.J.W., and C.K. Approval of submission: J.I.Y., R.M., Z.L., K.R.C-H., D.R., D.G., S.P.G.M., D.F., I.O.T. R.A.C., D.L., R.J.W., and C.K. Accountable for contributions: J.I.Y., R.M., Z.L., K.R.C-H., D.R., D.G., S.P.G.M., D.F., I.O.T. R.A.C., D.L., R.J.W., and C.K.

Declaration of interests

The authors declare no competing interests.

Methods

Experimental model and study participant details

Zebrafish husbandry

All zebrafish used in this study were bred and maintained at the University of Iowa Animal Care Facility. The zebrafish are kept consistently at 28 C, 7.4 pH, and controlled salt concentrations and cyclically receive 14 h of light followed by 10 hours of darkness. All zebrafish experiments were performed in compliance with the ethical regulations of the Institutional Animal Care and Use Committee at the University of Iowa and in compliance with NIH guidelines (protocol #3022523). Zebrafish embryos were maintained at 28.5°C and staged by hours or days post-fertilization (hpf or dpf).

Zebrafish mutant lines

Wild-type zebrafish in this study include the AB line and the WIK line. Transgenic lines include casper (*mitfa*$^{w2/w2}$,*mpv17*$^{-/-}$)[43,44], nacre (*mitfa*$^{w2/w2}$)[42], *Tg*(*mitfa*:GFP)[18], and *Tg*(*mitfa*:GFP); *mitfa*$^{w2/w2}$. TEAZ-Eye and TEAZ-Skin was performed on adult zebrafish (greater than 4 months postfertilization).

Cloning

The MiniCoopR vector (Plasmid #118844, addgene) was modified to replace the *mitfa* coding sequence with *GNAQ*^{Q209L} by first removing *mitfa* using StuI and SmaI restriction enzymes (NEB). Gibson assembly was used to insert *GNAQ*^{Q209L}:T2A:GFP DNA sequence as a gBlock hifi (IDT) with sequence on the 3' (GAAGCTAACACATAGTTGAAC) and 5' (CAATGCCAACTAAATTTCATG) end to match parts of the plasmid. Gibson assemblies were transformed into NEB 5-alpha competent *E. coli* cells via heat shock. We took *E. coli* colonies and partially confirmed insertion of *GNAQ*^{Q209L}:T2A:GFP using PCR amplification of lysed bacteria (forward primer: CAAGCTGGAGTACAACTACAA reverse primer:

ATAGGTGAATTGGGTAAGCTA). Positive products were isolated using the QIAGEN Plasmid Maxi Kit. The entire *GNAQ*^{Q209L}:T2A:GFP insertion was confirmed in purified DNA using sanger sequencing (Primers: CAAGGAAGCCCGGCGGATCAACGA, CATACTTGTATGGGATCTTGAGTGTGTCCA, GTGGAGTCAGACAATGAGAACCGAATGGAG, CAAGCTGGAGTACAACTACAA).

mitfa sgRNA was designed using IDT's CRISPR-Cas9 quide RNA design tool and has a sequence of: ATGGACAAAGCTGGACCATG. zfU6:sgRNA*ptena* was linearized by PCR (forward primer: U6 For GTTTAAGAGCTATGCTGGAAACAGCAT, reverse primer: U6 Rev GAACAAAGAGCTGGAGGGAG). Linear plasmid was purified from a 2% agarose gel using the Monarch GNA Gel Extraction Kit (#T1020S). ssDNA sequences for the sgRNA*mitfa* were annealed together in NE buffer r2.1. Gibson assembly was used to insert sgRNA*mitfa* into linearized U6 plasmid. Gibson assembly was transformed into NEB 5-alpha competent *E. coli* cells via heat shock and selected with 50 ug/mL streptomycin. We took *E. coli* colonies and partially confirmed insertion of sgRNA*mitfa* using PCR amplification of lysed bacteria (forward primer: mitfa_2_screen ATGGACAAAGCTGGACCATG, reverse primer: tp53_screen_Rev CTTAGCTGGATAACGCCAC). Positive products were isolated using the QIAGEN Plasmid Maxi Kit. Entire plasmid was sequenced using Plasmidsaurus sequencing service.

Transgene Electroporation of Adult Zebrafish Skin (TEAZ-Skin)

Adult zebrafish were anesthetized in 0.2% Tricaine prior to upright placement on a prewetted Kimwipe. Each injection consisted of 1000 ng total DNA: 100 ng of Tol2 plasmid and an equal division of the remaining 900 ng for the remaining constructs. Injection stocks contained a small volume (<1uL, 1:50 dilution) of green food coloring to visualize localization of injection. Injection volumes ranged from 1 to 1.5 uL depending on the injection mix, keeping 1000 ng total

constant. Needles were pulled from 10 cm long filamented borosilicate glass capillaries at a pressure of 500, heat of 650, pull strength of 100, velocity of 200, and time delay of 40 in a Model P-97 Flaming/Brown micropipette puller from Sutter Instrument Co. Following injection, zebrafish were immediately electroporated (<1 min) by placing the cathode probe of ultrasound gel-coated Platnium Tweezertrode, 3MM, on the side of the injection site and the anode probe on the other side of the fish body. Electroporation was achieved with 5 60 ms pulses of 40 volts with a 1s pulse interval from a ECM 830 Electro Square Porator from BTX Harvard Apparatus. Following electroporation, zebrafish are placed into a recovery tank with fresh, gently stirred system water and are monitored until normal swimming resumes. Electroporated zebrafish are imaged weekly for up to 70 weeks.

mitfa:*GNAQ*^{Q209L}; *mitfa*:GFP plasmid constructs were kindly provided by Dr. Jacqueline A. Lees (Massachusetts Institute of Technology, Cambridge, USA). *mitfa*:Cas9, *mitfa:*tdTomato, PCS2FA Tol2, *U6*:gRNA-*tp53, U6*:gRNA-*ptena,* and *U6*:gRNA-*ptenb* plasmids were kindly provided by Dr. Richard White (Sloan Kettering Institute, New York, USA).

Transgene Electroporation of Adult Zebrafish Eye (TEAZ-Eye)

Pre injection preparation for eye injections is the same as for skin injections including: 0.2% Tricaine anesthesia, zebrafish age, arrangement, needle size, and injection concentrations. To inject the eye, a blunt spherical head of a pin was gently pressed against the bottom half of the zebrafish eyeball to reveal the rear of the top of the eye. The needle was gently pressed into the top rear of the eye, where the cornea is softer, just through the sclera, keeping the needle as superficial as possible as to not damage the back of the eye. Injection volumes were around 0.25 uL and were terminated with a slight visual swelling of the eye. Following injection zebrafish were immediately electroporated (<1 min) by the cathode probe of ultrasound gel-

coated Platnium Tweezertrode, 1MM, on the superior side of the fish eye nearest the injection and the anode probe on the inferior side of the fish eye. Electroporation was achieved with 3 50ms pulses of 75 volts with a 1s pulse interval from a ECM 830 Electro Square Porator from BTX Harvard Apparatus. Recovery and imaging procedures for these fish did not differ from the skin injections.

GNAQ-B plasmid was kindly provided by Dr. Jacqueline A. Lees (Massachusetts Institute of Technology, Cambridge, USA). *mitfa*:Cas9, *mitfa:*tdTomato, PCS2FA Tol2, zU6-sgRNA*p53,* zU6-sgRNA*ptena,* and zU6-sgRNA*ptenb* plasmids were kindly provided by Dr. Richard White (Sloan Kettering Institute, New York, USA).

Imaging and image processing

All injected zebrafish were imaged using an upright Leica M205 FCA microscope with brightfield and GFP filters. Zebrafish were briefly anesthetized with 0.2% Tricaine and positioned on a Kimwipe mound for proper upright orientation. Images were taken and processed through the LAS X software. All histology slides were imaged using brightfield, DAPI, and GFP filters on an EVOS M5000 microscope from Invitrogen for individual images or on a Leica DMi8 microscope and stitched together by LAS X Thunder Imaging software for full tissue images.

Histology

Whole zebrafish or zebrafish eyes (punctured once) were fixed in 4% paraformaldehyde for 48 hours at 4 C and paraffin embedded in the University of Iowa Pathology Core. Fish were sectioned at 7 μM and placed on Superfrost Plus Microscope slides from Fisher Scientific, baked at 60 C, stained with hematoxylin and eosin, and mounted with Cytoseal 60 from

Epredia. For immunofluorescence, slides were stained with primary antibodies against GFP (NB600-308 Rabbit anti-GFP polyclonal from Novus Biologicals at 1:250) and then fluorescent secondary antibodies against rabbit IgG (Alexa Fluor 488 goat anti-rabbit IgG at 1:500 from a 2 mg/mL stock). RPE autofluorescence was minimized using the Vector TrueVIEW Autofluorescence Quenching Kit and slides were mounted using VECTASHIELD Vibrance Antifade Mounting Medium and imaged the same day.

Kaplan-Meier analysis

Zebrafish were followed for up to 70 weeks and tumor-free survival was analyzed with the Kaplan-Meier method. The differences between injection groups were analyzed using log-rank statistics.

Single cell suspension and single-cell RNA Seq analysis

Zebrafish were euthanized with 0.4% Tricaine for 10 mins followed by immersion in ice water until no opercular movement was observed for at least 10 min as detailed in the IACUC protocol. Tumors were harvested and minced into small pieces. Minced tumors were digested for 1 hour at 37 C with collagenase and hyaluronidase in HBSS with 2% FBS (HF). Suspensions were washed with 1:4 HF:NH_4Cl and then further digested for 5 min with pre-warmed trypsin. Following trypsin inactivation, cell suspensions were washed twice with 10% FBS in HBSS.

Cellular suspensions were loaded on a 10x Genomics Chromium instrument to generate single-cell gel beads in emulsion (GEMs). Approximately 10,000 cells were loaded per channel. Single-cell RNA-Seq libraries were prepared using Single Cell 3′ Reagent Kits v2: Chromium Single Cell 3′ Library & Gel Bead Kit v2, PN-120237; Single Cell 3′ Chip Kit v2 PN-120236 and i7

Multiplex Kit PN-120262 (10x Genomics) following the Single Cell 3′ Reagent Kits v2 User Guide (Manual Part # CG00052 Rev A). Libraries were run on an Illumina HiSeq 4000 as 2 × 150 paired-end reads. Sequencing results were demultiplexed and converted to FASTQ format using Illumina bcl2fastq software.

A custom reference genome for the Zebrafish was constructed with GRCz11 primary assembly (Ensembl) using Cell Ranger (Cell Ranger mkref function). 10X Genomics scRNA-seq reads were then processed and aligned to this reference with Cell Ranger (Cell Ranger Count function). Further analysis and visualization was performed using Seurat (v4.1.0)[71], cells with fewer than 200 RNA feature counts and greater than 5% mitochondrial contamination were removed with filtering (greater than 15% for wildtype eye tumor sample). RNA counts were normalized, and FindVariableFeatures was run with the following parameters: selection.method = “vst”, nfeatures = 2,000. The cells were originally clustered in a UMAP by RunPCA then RunUMAP with dims 1:30. FindNeighbors was run with dims 1:30 followed by FindClusters using a resolution of 0.4. These methods identified up to 20 clusters in individual samples.

For comparative analysis, RNA-seq datasets were integrated together using IntegrateData with dims 1:30. New clusters were generated as before. Clusters were annotated using FindAllMarkers and the top 25 enriched genes in each cluster were compared to the Daniocell dataset[72] and Spectacle[45]. Cluster names were given according to the closest matched cellular population between these two datasets. To determine enriched pathways, *danio rerio* gene names were converted into human Ensembl gene codes with g:Profiler[73] and then data were analyzed with the use of QIAGEN IPA (QIAGEN Inc)[74]. Pseudotime was performed using Monocle3 (v0.2.3.0)[75].

Verification of sgRNAs

Zebrafish were euthanized with 0.4% Tricaine for 10 mins followed by immersion in ice water until no opercular movement was observed for at least 10 min as detailed in the IACUC protocol. Tumors were harvested and minced into small pieces. DNA was harvested according to the DNeasy Blood and Tissue Kit from Qiagen. Regions surrounding cut sites were PCR-amplified and the presence of only the PCR amplicon of interest was confirmed with agarose gel electrophoresis. Samples were cleaned up with the QIAquick PCR Purification Kit from Qiagen and sent for Sanger sequencing at the Iowa Institute of Human Genetics. Cutting was confirmed with DECODR INDEL analysis by comparing to wildtype sequence[76]. PCR primer sequences follow:

mitfa PCR F: CCGGTATGTATTCACATTGTCTTG

mitfa PCR R: TCTTGCTTAGGATGCCTATGTATT

ptena PCR F: CATCCCACCAAGTGAGGTTAAAC

ptena PCR R: CACATACACAGTCAAGGGTGAG

ptenb PCR F: CAGTTCTGTTGCACCCAATAAG

ptenb PCR R: CTGGTGGTGTTGAGGCTATAAAG

tp53 PCR F: AAGTATTCAGCCCCCAGGTG

tp53 PCR R: CGCTTTTGACTCACAGTGCAAG

Figure 1: *GNAQ*^{Q209L}-induced melanoma by TEAZ-Skin.

(**A**) TEAZ-Skin was used to induce GNAQ-positive melanoma using two strategies. Strategy A involves a single plasmid construct containing expression cassettes driven by the *mitfa* promoter for GNAQ^{Q209L}-T2A-eGFP and Cas9, as well as a U6 promoter driving the expression of three separate gRNAs (targeting *tp53*, *ptena*, and *ptenb*, or a non-targeting control). Strategy B uses a multi-plasmid approach with five plasmids for TEAZ-Skin. Expression cassettes include: (a) *mitfa*:*GNAQ*^{Q209L}-*mitfa*:eGFP, (b) *U6*:gRNA (*tp53*), (c) *U6*:gRNA (*ptena*), and (d) *U6*:gRNA (*ptenb*).

(**B**) Schematic of TEAZ-Skin using wild type (AB), nacre (*mitfa*$^{w2/w2}$) and casper (*mitfa*$^{w2/w2}$*: mpv17*$^{a9/a9}$) zebrafish lines.

(**C**) TEAZ-Skin using Strategy B plasmids in adult wild-type (AB) zebrafish. Representative brightfield and fluorescent images shown at 4, 8 and 12 weeks post electroporation.

(**D**) Kaplan-Meier curves were used to estimate tumor-free survival in wild-type zebrafish defined as the time from electroporation until the first visible appearance of GFP+ nodular tumors. Experimental groups as labeled.

(**E**) TEAZ-Skin using Strategy B plasmids in adult nacre zebrafish. Representative brightfield and fluorescent images shown at 2, 4 and 6 weeks post electroporation.

(**F**) Kaplan-Meier curves were used to estimate tumor-free survival in nacre zebrafish defined as the time from electroporation until the first visible appearance of GFP+ nodular tumors. Experimental groups as labeled.

(**G**) TEAZ-Skin using Strategy B plasmids in adult casper zebrafish. Representative brightfield and fluorescent images shown at 2, 4 and 6 weeks post electroporation.

(**H**) Kaplan-Meier curves were used to estimate tumor-free survival in casper zebrafish defined as the time from electroporation until the first visible appearance of GFP+ nodular tumors. Experimental groups as labeled.

(**I-J**) Kaplan-Meier curves comparing tumor-free survival among wild-type, nacre, and casper zebrafish following TEAZ-Skin induction using Strategy B plasmids with (**I**) non-targeting control gRNAs and (**J**) gRNAs targeting *tp53, ptena* and *ptenb*. Experimental groups as labeled.

Figure 2: *GNAQ*^{Q209L}-induced uveal melanoma by TEAZ-Eye

(**A**) Schematic of the zebrafish eye, dashed box indicates the retina and choroid.

(**B**) H&E analysis of a wild type zebrafish eye (20x magnification). Eye structures as labeled with yellow asterisks marking choroidal melanocytes.

(**C–D**) Immunohistochemical analysis of transgenic *Tg(mitfa:GFP)* zebrafish using an anti-GFP antibody. Sections were counterstained with DAPI to visualize nuclei. (**C**) Representative image showing GFP expression in *mitfa*-positive cells. (**D**) Secondary-only antibody was used as background control.

(**E**) Schematic of TEAZ-Eye using choroidal targeted injection of Strategy B plasmids.

(**F-K, F'-K'**) Live imaging of adult wild-type zebrafish over 42 days post-electroporation (dpe) using the TEAZ-Eye method with Strategy B plasmids to induce uveal melanoma. (F-K) brightfield imaging and (F'-K') the corresponding GFP fluorescence images highlighting tumor progression.

(**L-N, L'-N'**) Live imaging of adult casper zebrafish over 21 days post-electroporation (dpe) using the TEAZ-Eye method with Strategy B plasmids to induce uveal melanoma. (L-N) brightfield imaging and (L'-N') the corresponding GFP fluorescence images highlighting tumor progression.

(**O**) H&E analysis of uveal melanoma in casper zebrafish induced by TEAZ-Eye. Images were acquired at 20× magnification and stitched from 85 fields using Thunder imaging software. Normal eye tissue and uveal melanoma as labeled.

(**P-Q**) anti-GFP immunohistochemical analysis of TEAZ-Eye induced uveal melanoma. Sections were counterstained with DAPI to visualize nuclei. (P) Images were acquired at 20×

magnification and stitched from 85 fields using Thunder imaging software. (Q) Representative 40x magnification image showing GFP expression in tumors cells.

Figure 3: Single cell profiling of uveal melanoma in adult zebrafish.

(**A**) Representative brightfield and GFP overlap image of TEAZ-Eye (Strategy B) induced uveal melanoma in a wild-type zebrafish at 50 days post electroporation (dpe).

(**B-C**) UMAP representation of single cell RNA-Seq (scRNA-Seq) from three dissociated wild-type eyes harboring UM tumors generated via TEAZ-Eye. Annotated cell clusters as labeled.

(C) UMAP and feature plot showing *eGFP* expression in UM tumors cells.

(**D**) Dot plot showing enriched genes (log2FC > 2; FDR < 0.05) in choroidal cell populations, UM tumors cells, immune cell populations, fibroblasts, and endothelial cells as shown. Dot size indicates the percentage of cells expressing each gene; color intensity (grey to blue) reflects normalized average expression levels (low to high).

(**E**) Representative brightfield and GFP overlap image of TEAZ-Skin (Strategy B) induced melanoma in a wild-type zebrafish at 60 days post electroporation (dpe).

(**F**) UMAP representation of scRNA-seq data from TEAZ-Eye and TEAZ-Skin wild-type zebrafish. Eye tumor cells are highlighted in red and eye tumor microenvironment (TME) cells in dark grey; skin tumor cells are shown in blue and skin TME cells in light grey.

(**G-G'**) Re-clustered UMAP representing GFP-positive eye and skin tumor cells.

(G') Venn diagram showing overlapping genes between eye- and skin-derived GNAQ+ tumors. Prior to overlap analysis, enriched genes for each tumor type were identified by differential expression analysis comparing tumor cells to their respective tumor microenvironment (TME), using a threshold of log2FC > 1 and FDR < 0.05.

(**H**) Dot plot showing differentiational expressed genes (log2FC > 2; FDR < 0.05) between Eye and Skin derived tumors. Dot size indicates the percentage of cells expressing each gene; color intensity (grey to blue) reflects normalized average expression levels (low to high).

(**I–I'**) Kaplan–Meier disease-free survival curves generated using TCGA data.

(I) Uveal melanoma and (I') cutaneous melanoma patients stratified by relative expression levels of *KIT* and *FABP3*. High expression groups are shown in red; low expression groups in blue. Gene expression thresholds were defined by median expression within each cohort. Log rank p-values as shown. Dotted lines represent 95% confidence interval.

(**J-J'**) Kaplan–Meier overall survival curves generated using TCGA data. (J) Uveal melanoma and (J') cutaneous melanoma patients stratified by relative expression levels of *LGALS2*. Gene expression thresholds were defined by median expression within each cohort. Log rank p-values as shown. Dotted lines represent 95% confidence interval.

Figure 4: *mitf*-independent melanocyte progenitor cells are expanded in *mitfa*-deficient zebrafish and are susceptible to *GNAQ*^{Q209L} transformation.

(**A**) Kaplan-Meier curves comparing tumor-free survival among wild-type, nacre, and casper zebrafish following TEAZ-Eye induction using Strategy B plasmids.

(**B**) H&E analysis showing the retina and choroid of wild-type (left) and nacre (right) zebrafish eyes (20x magnification). Note the loss of melanocytes in the choroid of nacre eyes.

(**C**) Immunohistochemical analysis of transgenic *Tg(mitfa:GFP); mitfa*$^{w2/w2}$ (nacre) zebrafish using an anti-GFP antibody. Sections were counterstained with DAPI to visualize nuclei. Representative images showing GFP positive cells in the ciliary body and choroid are shown by yellow arrow heads. Secondary-only antibody was used as background control.

(**D**) UMAP representation of single-cell RNA sequencing (scRNA-Seq) data from three dissociated control-injected eyes (*mitfa*:Cas9 with non-targeting gRNAs) and from eyes

harboring uveal melanoma (UM) tumors induced using Strategy B via TEAZ-Eye. Annotated cell clusters are labeled. Progenitor cells and UM tumor clusters are outlined with dashed red lines. Representative brightfield images of a normal eye and a UM tumor in casper zebrafish are shown in the top left corner of the UMAP.

(**E**) Re-clustered UMAP representing progenitor cells from control eyes and uveal melanoma (UM) tumor cells from TEAZ-Eye–injected casper zebrafish. Heterogeneous cell populations as labeled.

(**F**) Re-clustered UMAP from (E) showing melanocyte progenitor cells from control eyes in red and UM tumor cells from TEAZ-Eye in blue. Expression plots for *pax3a, foxd3* and *sox10* are shown, dashed line marks the progenitor cell population.

(**G**) Dot plot illustrating differentiational expressed genes (log2FC > 2; FDR < 0.05) between heterogeneous cell populations in (E). Dot size indicates the percentage of cells expressing each gene; color intensity (blue to red) reflects normalized average expression levels (low to high).

(**H**) UMAP obtained after clustering GFP-positive cells sorted from *Tg(mitfa:GFP)* and *Tg(mitfa:GFP); mitfa*$^{w2/w2}$ (nacre) zebrafish embryos at 28 hours post fertilization (hpf). Annotated cell clusters as labelled.

(**I**) Comparison of relative cluster size for the two genotypes; *Tg(mitfa:GFP)* and *Tg(mitfa:GFP); mitfa*$^{w2/w2}$ (nacre) in (H).

(**J**) Dot plot illustrating differentiational expressed genes (log2FC > 2; FDR < 0.05) in melanophores and progenitor cells in *mitfa*$^{w2/w2}$ and sibling embryos at 28hpf. Dot size indicates the percentage of cells expressing each gene; color intensity (grey to red) reflects normalized average expression levels (low to high).

(**K-K'**) Kaplan–Meier curves comparing tumor-free survival in wild-type (n=12) and casper (n=6) zebrafish following TEAZ-Eye injection using Strategy B plasmids.

Wild-type zebrafish were injected with either Strategy B plasmids plus non-targeting gRNAs (n=6) or Strategy B plasmids plus *mitfa*-targeting gRNAs (n=6). Casper zebrafish were injected with Strategy B plasmids and *mitfa*-targeting gRNAs (n=6). (**K'**) Representative brightfield and GFP-overlay images of tumors that formed in casper (6 of 6) and wild-type zebrafish injected with *mitfa*-targeting gRNAs (1 of 6). Metastatic cells are indicated by red arrows.

Figure 5: Oncogenic GNAQ and BRAF transform transcriptionally distinct cells within the melanocyte lineage.

(**A**) UMAP obtained after clustering tumor cells from *Tg(mitfa:BRAF^{v600e}): tp53$^{-/-}$* : *mitfa$^{w2/w2}$* zebrafish where TEAZ-Skin was used to rescue *mitfa* expression and knockout *ptena* and *ptenb* to induce cutaneous melanoma[29], along with our GNAQ-induced tumors by TEAZ-Skin (Strategy B: *mitfa:Cas9, U6:*gRNA-*tp53, U6:*gRNA-*ptena, U6:*gRNA-*ptenb, mitfa:GNAQ^{Q209L}-mitfa:GFP*). BRAF-induced tumors in red and GNAQ-induced tumors in blue.

(**B**) Violin plot showing differentially expressed genes (log2FC > |1|, FDR < 0.05) between BRAF-induced and GNAQ-induced tumors from (A). The plot displays the distribution of gene expression across individual cells, with the width indicating cell density at specific expression levels and the height representing the range of expression values.

(**C**) Integrated UMAP after clustering GFP-positive cells sorted from *Tg(mitfa:GFP)* and *Tg(mitfa:GFP); mitfa$^{w2/w2}$* (nacre) zebrafish embryos at 28 hours post fertilization (hpf). Annotated cell clusters as labelled.

(**D**) Enrichment of signature genes from BRAF- and GNAQ-driven tumors projected onto the UMAP in (C) using UCell and the 'FeaturePlot' function. Signature genes represent the top 50 enriched genes from each tumor genotype that are also expressed in the embryonic melanocyte lineage.

Figure S1: Immunohistochemistry of the choroid using anti-GFP antibody in *Tg*(*mitfa*:GFP) and TEAZ-Eye injected zebrafish.

Figure S2: UMAP of *GNAQ*^{Q209L}-induced tumors by TEAZ-Eye and TEAZ-Skin in wild-type zebrafish (Strategy B).

Figure S3: Ingenuity Pathway Analysis (IPA) of TEAZ-Eye and TEAZ-Skin tumors versus their respective TME (Enriched in TEAZ-Eye).

Figure S4: Ingenuity Pathway Analysis (IPA) of TEAZ-Eye tumors verses TME.

Figure S5: Ingenuity Pathway Analysis (IPA) of TEAZ-Eye and TEAZ-Skin tumors versus their respective TME (Enriched in TEAZ-Skin).

Figure S6: Overall survival of patients with uveal melanoma (UM) and cutaneous melanoma (CM) based on expression levels of *FABP3*, *FABP5*, and *KIT*. Disease-free survival in UM and CM patients based on *FABP5* expression. Dotted lines represent 95% confidence intervals. Data derived from TCGA datasets.

Figure S7: Melanocyte rescue nacre zebrafish by TEAZ-Eye using plasmids containing *mitfa*:*mitfa*; *mitfa*:GFP (miniCoopR)

Figure S8: UMAP representation of UM tumors derived from casper zebrafish, with accompanying pseudotime analysis.

Figure S9: Immunohistochemical staining for Pax3 in the mouse limbus.

Figure S10: Representative images of TEAZ-Skin induced tumors (*Strategy B*) in wild-type, conditional *mitfa*-KO (wild-type) and casper zebrafish.

Figure S11: Violin plots of *mitfa* and Mitfa-target genes in BRAF and GNAQ derived tumors by scRNA-Seq analysis.

Figure S12: Dot plot of pigment cell genes that are enriched in UM tumors derived by TEAZ-Eye in wild-type zebrafish.

1. Gentien, D., Saberi-Ansari, E., Servant, N., Jolly, A., de la Grange, P., Némati, F., Liot, G., Saule, S., Teissandier, A., Bourc'his, D., et al. (2023). Multi-omics comparison of malignant and normal uveal melanocytes reveals molecular features of uveal melanoma. Cell Rep *42*, 113132. 10.1016/j.celrep.2023.113132.
2. Rodrigues, M., Mobuchon, L., Houy, A., Alsafadi, S., Baulande, S., Mariani, O., Marande, B., Ait Rais, K., Van der Kooij, M.K., Kapiteijn, E., et al. (2019). Evolutionary Routes in Metastatic Uveal Melanomas Depend on MBD4 Alterations. Clin Cancer Res *25*, 5513-5524. 10.1158/1078-0432.Ccr-19-1215.
3. Kolandjian, N.A., Wei, C., Patel, S.P., Richard, J.L., Dett, T., Papadopoulos, N.E., and Bedikian, A.Y. (2013). Delayed systemic recurrence of uveal melanoma. Am J Clin Oncol *36*, 443-449. 10.1097/COC.0b013e3182546a6b.
4. Lamas, N.J., Martel, A., Nahon-Estève, S., Goffinet, S., Macocco, A., Bertolotto, C., Lassalle, S., and Hofman, P. (2021). Prognostic Biomarkers in Uveal Melanoma: The Status Quo, Recent Advances and Future Directions. Cancers (Basel) *14*. 10.3390/cancers14010096.
5. Eskelin, S., and Kivelä, T. (2002). Mode of presentation and time to treatment of uveal melanoma in Finland. Br J Ophthalmol *86*, 333-338. 10.1136/bjo.86.3.333.
6. Carvajal, R.D., Schwartz, G.K., Tezel, T., Marr, B., Francis, J.H., and Nathan, P.D. (2017). Metastatic disease from uveal melanoma: treatment options and future prospects. Br J Ophthalmol *101*, 38-44. 10.1136/bjophthalmol-2016-309034.
7. Jager, M.J., Shields, C.L., Cebulla, C.M., Abdel-Rahman, M.H., Grossniklaus, H.E., Stern, M.H., Carvajal, R.D., Belfort, R.N., Jia, R., Shields, J.A., and Damato, B.E. (2020). Uveal melanoma. Nat Rev Dis Primers *6*, 24. 10.1038/s41572-020-0158-0.
8. Wessely, A., Steeb, T., Erdmann, M., Heinzerling, L., Vera, J., Schlaak, M., Berking, C., and Heppt, M.V. (2020). The Role of Immune Checkpoint Blockade in Uveal Melanoma. Int J Mol Sci *21*. 10.3390/ijms21030879.
9. Bauer, S., Larkin, J., Hodi, F.S., Stephen, F., Kapiteijn, E.H.W., Schwartz, G.K., Calvo, E., Yerramilli-Rao, P., Piperno-Neumann, S., and Carvajal, R.D. (2022). A phase Ib trial of combined PKC and MEK inhibition with sotrastaurin and binimetinib in patients with metastatic uveal melanoma. Front Oncol *12*, 975642. 10.3389/fonc.2022.975642.
10. Gragoudas, E.S., Egan, K.M., Seddon, J.M., Glynn, R.J., Walsh, S.M., Finn, S.M., Munzenrider, J.E., and Spar, M.D. (1991). Survival of patients with metastases from uveal melanoma. Ophthalmology *98*, 383-389; discussion 390. 10.1016/s0161-6420(91)32285-1.
11. Rantala, E.S., Hernberg, M., and Kivelä, T.T. (2019). Overall survival after treatment for metastatic uveal melanoma: a systematic review and meta-analysis. Melanoma Res *29*, 561-568. 10.1097/cmr.0000000000000575.
12. Leiter, U., Meier, F., Schittek, B., and Garbe, C. (2004). The natural course of cutaneous melanoma. J Surg Oncol *86*, 172-178. 10.1002/jso.20079.
13. Eggermont, A.M., Spatz, A., and Robert, C. (2014). Cutaneous melanoma. Lancet *383*, 816-827. 10.1016/s0140-6736(13)60802-8.
14. Breslow, A. (1970). Thickness, cross-sectional areas and depth of invasion in the prognosis of cutaneous melanoma. Ann Surg *172*, 902-908. 10.1097/00000658-197011000-00017.

15. Davies, M.A., Liu, P., McIntyre, S., Kim, K.B., Papadopoulos, N., Hwu, W.J., Hwu, P., and Bedikian, A. (2011). Prognostic factors for survival in melanoma patients with brain metastases. Cancer *117*, 1687-1696. 10.1002/cncr.25634.
16. Fischer, G.M., Jalali, A., Kircher, D.A., Lee, W.C., McQuade, J.L., Haydu, L.E., Joon, A.Y., Reuben, A., de Macedo, M.P., Carapeto, F.C.L., et al. (2019). Molecular Profiling Reveals Unique Immune and Metabolic Features of Melanoma Brain Metastases. Cancer Discov *9*, 628-645. 10.1158/2159-8290.Cd-18-1489.
17. Shain, A.H., Bagger, M.M., Yu, R., Chang, D., Liu, S., Vemula, S., Weier, J.F., Wadt, K., Heegaard, S., Bastian, B.C., and Kiilgaard, J.F. (2019). The genetic evolution of metastatic uveal melanoma. Nat Genet *51*, 1123-1130. 10.1038/s41588-019-0440-9.
18. Silva-Rodríguez, P., Fernández-Díaz, D., Bande, M., Pardo, M., Loidi, L., and Blanco-Teijeiro, M.J. (2022). GNAQ and GNA11 Genes: A Comprehensive Review on Oncogenesis, Prognosis and Therapeutic Opportunities in Uveal Melanoma. Cancers (Basel) *14*. 10.3390/cancers14133066.
19. Li, Y., Shi, J., Yang, J., Ge, S., Zhang, J., Jia, R., and Fan, X. (2020). Uveal melanoma: progress in molecular biology and therapeutics. Ther Adv Med Oncol *12*, 1758835920965852. 10.1177/1758835920965852.
20. Ma, J., Weng, L., Bastian, B.C., and Chen, X. (2021). Functional characterization of uveal melanoma oncogenes. Oncogene *40*, 806-820. 10.1038/s41388-020-01569-5.
21. Livingstone, E., Zaremba, A., Horn, S., Ugurel, S., Casalini, B., Schlaak, M., Hassel, J.C., Herbst, R., Utikal, J.S., Weide, B., et al. (2020). GNAQ and GNA11 mutant nonuveal melanoma: a subtype distinct from both cutaneous and uveal melanoma. Br J Dermatol *183*, 928-939. 10.1111/bjd.18947.
22. Lee, J.H., Choi, J.W., and Kim, Y.S. (2011). Frequencies of BRAF and NRAS mutations are different in histological types and sites of origin of cutaneous melanoma: a meta-analysis. Br J Dermatol *164*, 776-784. 10.1111/j.1365-2133.2010.10185.x.
23. Urtatiz, O., Haage, A., Tanentzapf, G., and Van Raamsdonk, C.D. (2021). Crosstalk with keratinocytes causes GNAQ oncogene specificity in melanoma. Elife *10*. 10.7554/eLife.71825.
24. Callahan, S.J., Tepan, S., Zhang, Y.M., Lindsay, H., Burger, A., Campbell, N.R., Kim, I.S., Hollmann, T.J., Studer, L., Mosimann, C., and White, R.M. (2018). Cancer modeling by Transgene Electroporation in Adult Zebrafish (TEAZ). Dis Model Mech *11*. 10.1242/dmm.034561.
25. Brombin, A., Simpson, D.J., Travnickova, J., Brunsdon, H., Zeng, Z., Lu, Y., Young, A.I.J., Chandra, T., and Patton, E.E. (2022). Tfap2b specifies an embryonic melanocyte stem cell that retains adult multifate potential. Cell Rep *38*, 110234. 10.1016/j.celrep.2021.110234.
26. Ceol, C.J., Houvras, Y., Jane-Valbuena, J., Bilodeau, S., Orlando, D.A., Battisti, V., Fritsch, L., Lin, W.M., Hollmann, T.J., Ferré, F., et al. (2011). The histone methyltransferase SETDB1 is recurrently amplified in melanoma and accelerates its onset. Nature *471*, 513-517. 10.1038/nature09806.
27. Kenny, C., Dilshat, R., Seberg, H.E., Van Otterloo, E., Bonde, G., Helverson, A., Franke, C.M., Steingrímsson, E., and Cornell, R.A. (2022). TFAP2 paralogs facilitate chromatin

access for MITF at pigmentation and cell proliferation genes. PLoS Genet *18*, e1010207. 10.1371/journal.pgen.1010207.
28. Lister, J.A., Lane, B.M., Nguyen, A., and Lunney, K. (2011). Embryonic expression of zebrafish MiT family genes tfe3b, tfeb, and tfec. Dev Dyn *240*, 2529-2538. 10.1002/dvdy.22743.
29. Lumaquin-Yin, D., Montal, E., Johns, E., Baggiolini, A., Huang, T.H., Ma, Y., LaPlante, C., Suresh, S., Studer, L., and White, R.M. (2023). Lipid droplets are a metabolic vulnerability in melanoma. Nat Commun *14*, 3192. 10.1038/s41467-023-38831-9.
30. Petratou, K., Spencer, S.A., Kelsh, R.N., and Lister, J.A. (2021). The MITF paralog tfec is required in neural crest development for fate specification of the iridophore lineage from a multipotent pigment cell progenitor. PLoS One *16*, e0244794. 10.1371/journal.pone.0244794.
31. Phelps, G.B., Hagen, H.R., Amsterdam, A., and Lees, J.A. (2022). MITF deficiency accelerates GNAQ-driven uveal melanoma. Proc Natl Acad Sci U S A *119*, e2107006119. 10.1073/pnas.2107006119.
32. Seberg, H.E., Van Otterloo, E., Loftus, S.K., Liu, H., Bonde, G., Sompallae, R., Gildea, D.E., Santana, J.F., Manak, J.R., Pavan, W.J., et al. (2017). TFAP2 paralogs regulate melanocyte differentiation in parallel with MITF. PLoS Genet *13*, e1006636. 10.1371/journal.pgen.1006636.
33. Kelsh, R.N., Brand, M., Jiang, Y.J., Heisenberg, C.P., Lin, S., Haffter, P., Odenthal, J., Mullins, M.C., van Eeden, F.J., Furutani-Seiki, M., et al. (1996). Zebrafish pigmentation mutations and the processes of neural crest development. Development *123*, 369-389. 10.1242/dev.123.1.369.
34. Dutton, K.A., Pauliny, A., Lopes, S.S., Elworthy, S., Carney, T.J., Rauch, J., Geisler, R., Haffter, P., and Kelsh, R.N. (2001). Zebrafish colourless encodes sox10 and specifies non-ectomesenchymal neural crest fates. Development *128*, 4113-4125. 10.1242/dev.128.21.4113.
35. McGowan, K.A., and Barsh, G.S. (2016). Evolution: How the zebrafish got its stripes. Elife *5*. 10.7554/eLife.14239.
36. Parichy, D.M., and Spiewak, J.E. (2015). Origins of adult pigmentation: diversity in pigment stem cell lineages and implications for pattern evolution. Pigment Cell Melanoma Res *28*, 31-50. 10.1111/pcmr.12332.
37. Phelps, G.B., Amsterdam, A., Hagen, H.R., García, N.Z., and Lees, J.A. (2022). MITF deficiency and oncogenic GNAQ each promote proliferation programs in zebrafish melanocyte lineage cells. Pigment Cell Melanoma Res *35*, 539-547. 10.1111/pcmr.13057.
38. Wessely, A., Steeb, T., Berking, C., and Heppt, M.V. (2021). How Neural Crest Transcription Factors Contribute to Melanoma Heterogeneity, Cellular Plasticity, and Treatment Resistance. Int J Mol Sci *22*. 10.3390/ijms22115761.
39. Kaufman, C.K., Mosimann, C., Fan, Z.P., Yang, S., Thomas, A.J., Ablain, J., Tan, J.L., Fogley, R.D., van Rooijen, E., Hagedorn, E.J., et al. (2016). A zebrafish melanoma model reveals emergence of neural crest identity during melanoma initiation. Science *351*, aad2197. 10.1126/science.aad2197.
40. Lister, J.A., Capper, A., Zeng, Z., Mathers, M.E., Richardson, J., Paranthaman, K., Jackson, I.J., and Elizabeth Patton, E. (2014). A conditional zebrafish MITF mutation reveals MITF

levels are critical for melanoma promotion vs. regression in vivo. J Invest Dermatol *134*, 133-140. 10.1038/jid.2013.293.

41. Travnickova, J., Wojciechowska, S., Khamseh, A., Gautier, P., Brown, D.V., Lefevre, T., Brombin, A., Ewing, A., Capper, A., Spitzer, M., et al. (2019). Zebrafish MITF-Low Melanoma Subtype Models Reveal Transcriptional Subclusters and MITF-Independent Residual Disease. Cancer Res *79*, 5769-5784. 10.1158/0008-5472.Can-19-0037.
42. Lister, J.A., Robertson, C.P., Lepage, T., Johnson, S.L., and Raible, D.W. (1999). nacre encodes a zebrafish microphthalmia-related protein that regulates neural-crest-derived pigment cell fate. Development *126*, 3757-3767. 10.1242/dev.126.17.3757.
43. D'Agati, G., Beltre, R., Sessa, A., Burger, A., Zhou, Y., Mosimann, C., and White, R.M. (2017). A defect in the mitochondrial protein Mpv17 underlies the transparent casper zebrafish. Dev Biol *430*, 11-17. 10.1016/j.ydbio.2017.07.017.
44. White, R.M., Sessa, A., Burke, C., Bowman, T., LeBlanc, J., Ceol, C., Bourque, C., Dovey, M., Goessling, W., Burns, C.E., and Zon, L.I. (2008). Transparent adult zebrafish as a tool for in vivo transplantation analysis. Cell Stem Cell *2*, 183-189. 10.1016/j.stem.2007.11.002.
45. Voigt, A.P., Whitmore, S.S., Lessing, N.D., DeLuca, A.P., Tucker, B.A., Stone, E.M., Mullins, R.F., and Scheetz, T.E. (2020). Spectacle: An interactive resource for ocular single-cell RNA sequencing data analysis. Exp Eye Res *200*, 108204. 10.1016/j.exer.2020.108204.
46. Voigt, A.P., Mulfaul, K., Mullin, N.K., Flamme-Wiese, M.J., Giacalone, J.C., Stone, E.M., Tucker, B.A., Scheetz, T.E., and Mullins, R.F. (2019). Single-cell transcriptomics of the human retinal pigment epithelium and choroid in health and macular degeneration. Proc Natl Acad Sci U S A *116*, 24100-24107. 10.1073/pnas.1914143116.
47. Howe, D.G., Bradford, Y.M., Conlin, T., Eagle, A.E., Fashena, D., Frazer, K., Knight, J., Mani, P., Martin, R., Moxon, S.A., et al. (2013). ZFIN, the Zebrafish Model Organism Database: increased support for mutants and transgenics. Nucleic Acids Res *41*, D854-860. 10.1093/nar/gks938.
48. Baggiolini, A., Callahan, S.J., Montal, E., Weiss, J.M., Trieu, T., Tagore, M.M., Tischfield, S.E., Walsh, R.M., Suresh, S., Fan, Y., et al. (2021). Developmental chromatin programs determine oncogenic competence in melanoma. Science *373*, eabc1048. 10.1126/science.abc1048.
49. Johns, E., Ma, Y., Louphrasitthiphol, P., Peralta, C., Hunter, M.V., Raymond, J.H., Molina, H., Goding, C.R., and White, R.M. (2025). The Lipid Droplet Protein DHRS3 Is a Regulator of Melanoma Cell State. Pigment Cell Melanoma Res *38*, e13208. 10.1111/pcmr.13208.
50. Xu, Y., Xu, W.H., Yang, X.L., Zhang, H.L., and Zhang, X.F. (2020). Fatty acid-binding protein 5 predicts poor prognosis in patients with uveal melanoma. Oncol Lett *19*, 1771-1780. 10.3892/ol.2020.11301.
51. Van Ly, D., Wang, D., Conway, R.M., Giblin, M., Liang, S., Lukeis, R., Lim, L.A., Hesson, L., and Cherepanoff, S. (2020). Lipid-Producing Ciliochoroidal Melanoma with Expression of HMG-CoA Reductase. Ocul Oncol Pathol *6*, 416-421. 10.1159/000510393.
52. Yavuzyigitoglu, S., Kilic, E., Vaarwater, J., de Klein, A., Paridaens, D., and Verdijk, R.M. (2016). Lipomatous Change in Uveal Melanoma: Histopathological, Immunohistochemical and Cytogenetic Analysis. Ocul Oncol Pathol *2*, 133-135. 10.1159/000440981.

53. Fiorentzis, M., Kalirai, H., Katopodis, P., and Coupland, S.E. (2017). Adipophilin expression in primary and metastatic uveal melanoma: a pilot study. Graefes Arch Clin Exp Ophthalmol *255*, 1049-1051. 10.1007/s00417-017-3630-0.
54. Feng, X., Degese, M.S., Iglesias-Bartolome, R., Vaque, J.P., Molinolo, A.A., Rodrigues, M., Zaidi, M.R., Ksander, B.R., Merlino, G., Sodhi, A., et al. (2014). Hippo-independent activation of YAP by the GNAQ uveal melanoma oncogene through a trio-regulated rho GTPase signaling circuitry. Cancer Cell *25*, 831-845. 10.1016/j.ccr.2014.04.016.
55. Boru, G., Cebulla, C.M., Sample, K.M., Massengill, J.B., Davidorf, F.H., and Abdel-Rahman, M.H. (2019). Heterogeneity in Mitogen-Activated Protein Kinase (MAPK) Pathway Activation in Uveal Melanoma With Somatic GNAQ and GNA11 Mutations. Invest Ophthalmol Vis Sci *60*, 2474-2480. 10.1167/iovs.18-26452.
56. Mouti, M.A., Dee, C., Coupland, S.E., and Hurlstone, A.F. (2016). Minimal contribution of ERK1/2-MAPK signalling towards the maintenance of oncogenic GNAQQ209P-driven uveal melanomas in zebrafish. Oncotarget *7*, 39654-39670. 10.18632/oncotarget.9207.
57. Horvathova Kajabova, V., Soltysova, A., Demkova, L., Plesnikova, P., Lyskova, D., Furdova, A., Babal, P., and Smolkova, B. (2021). KIT Expression Is Regulated by DNA Methylation in Uveal Melanoma Tumors. Int J Mol Sci *22*. 10.3390/ijms221910748.
58. Han, A., Purwin, T.J., Bechtel, N., Liao, C., Chua, V., Seifert, E., Sato, T., Schug, Z.T., Speicher, D.W., Harbour, J.W., and Aplin, A.E. (2021). BAP1 mutant uveal melanoma is stratified by metabolic phenotypes with distinct vulnerability to metabolic inhibitors. Oncogene *40*, 618-632. 10.1038/s41388-020-01554-y.
59. Matatall, K.A., Agapova, O.A., Onken, M.D., Worley, L.A., Bowcock, A.M., and Harbour, J.W. (2013). BAP1 deficiency causes loss of melanocytic cell identity in uveal melanoma. BMC Cancer *13*, 371. 10.1186/1471-2407-13-371.
60. Chang, J., Campbell-Hanson, K.R., Vanneste, M., Bartschat, N.I., Nagel, R., Arnadottir, A.K., Vu, H.N., Montgomery, C., Yevdash, J., Jiang, J., et al. (2025). Antagonistic roles for MITF and TFE3 in melanoma plasticity. Cell Rep *44*, 115474. 10.1016/j.celrep.2025.115474.
61. Hajkova, N., Hojny, J., Nemejcova, K., Dundr, P., Ulrych, J., Jirsova, K., Glezgova, J., and Ticha, I. (2018). Germline mutation in the TP53 gene in uveal melanoma. Sci Rep *8*, 7618. 10.1038/s41598-018-26040-0.
62. Abdel-Rahman, M.H., Yang, Y., Zhou, X.P., Craig, E.L., Davidorf, F.H., and Eng, C. (2006). High frequency of submicroscopic hemizygous deletion is a major mechanism of loss of expression of PTEN in uveal melanoma. J Clin Oncol *24*, 288-295. 10.1200/jco.2005.02.2418.
63. Harbour, J.W., Onken, M.D., Roberson, E.D., Duan, S., Cao, L., Worley, L.A., Council, M.L., Matatall, K.A., Helms, C., and Bowcock, A.M. (2010). Frequent mutation of BAP1 in metastasizing uveal melanomas. Science *330*, 1410-1413. 10.1126/science.1194472.
64. Brantley, M.A., Jr., and Harbour, J.W. (2000). Deregulation of the Rb and p53 pathways in uveal melanoma. Am J Pathol *157*, 1795-1801. 10.1016/s0002-9440(10)64817-1.
65. Coupland, S.E., Anastassiou, G., Stang, A., Schilling, H., Anagnostopoulos, I., Bornfeld, N., and Stein, H. (2000). The prognostic value of cyclin D1, p53, and MDM2 protein expression in uveal melanoma. J Pathol *191*, 120-126. 10.1002/(sici)1096-9896(200006)191:2<120::Aid-path591>3.0.Co;2-p.

66. Paraoan, L., Gray, D., Hiscott, P., Ebrahimi, B., Damato, B., and Grierson, I. (2006). Expression of p53-induced apoptosis effector PERP in primary uveal melanomas: downregulation is associated with aggressive type. Exp Eye Res *83*, 911-919. 10.1016/j.exer.2006.04.016.
67. Davies, L., Spiller, D., White, M.R., Grierson, I., and Paraoan, L. (2011). PERP expression stabilizes active p53 via modulation of p53-MDM2 interaction in uveal melanoma cells. Cell Death Dis *2*, e136. 10.1038/cddis.2011.19.
68. de Lange, J., Ly, L.V., Lodder, K., Verlaan-de Vries, M., Teunisse, A.F., Jager, M.J., and Jochemsen, A.G. (2012). Synergistic growth inhibition based on small-molecule p53 activation as treatment for intraocular melanoma. Oncogene *31*, 1105-1116. 10.1038/onc.2011.309.
69. Pópulo, H., Soares, P., Rocha, A.S., Silva, P., and Lopes, J.M. (2010). Evaluation of the mTOR pathway in ocular (uvea and conjunctiva) melanoma. Melanoma Res *20*, 107-117. 10.1097/CMR.0b013e32832ccd09.
70. Woodman, S.E. (2012). Metastatic uveal melanoma: biology and emerging treatments. Cancer J *18*, 148-152. 10.1097/PPO.0b013e31824bd256.
71. Butler, A., Hoffman, P., Smibert, P., Papalexi, E., and Satija, R. (2018). Integrating single-cell transcriptomic data across different conditions, technologies, and species. Nat Biotechnol *36*, 411-420. 10.1038/nbt.4096.
72. Sur, A., Wang, Y., Capar, P., Margolin, G., Prochaska, M.K., and Farrell, J.A. (2023). Single-cell analysis of shared signatures and transcriptional diversity during zebrafish development. Dev Cell *58*, 3028-3047.e3012. 10.1016/j.devcel.2023.11.001.
73. Kolberg, L., Raudvere, U., Kuzmin, I., Adler, P., Vilo, J., and Peterson, H. (2023). g:Profiler-interoperable web service for functional enrichment analysis and gene identifier mapping (2023 update). Nucleic Acids Res *51*, W207-w212. 10.1093/nar/gkad347.
74. Krämer, A., Green, J., Pollard, J., Jr., and Tugendreich, S. (2014). Causal analysis approaches in Ingenuity Pathway Analysis. Bioinformatics *30*, 523-530. 10.1093/bioinformatics/btt703.
75. Trapnell, C., Cacchiarelli, D., Grimsby, J., Pokharel, P., Li, S., Morse, M., Lennon, N.J., Livak, K.J., Mikkelsen, T.S., and Rinn, J.L. (2014). The dynamics and regulators of cell fate decisions are revealed by pseudotemporal ordering of single cells. Nat Biotechnol *32*, 381-386. 10.1038/nbt.2859.
76. Bloh, K., Kanchana, R., Bialk, P., Banas, K., Zhang, Z., Yoo, B.C., and Kmiec, E.B. (2021). Deconvolution of Complex DNA Repair (DECODR): Establishing a Novel Deconvolution Algorithm for Comprehensive Analysis of CRISPR-Edited Sanger Sequencing Data. Crispr j *4*, 120-131. 10.1089/crispr.2020.0022.

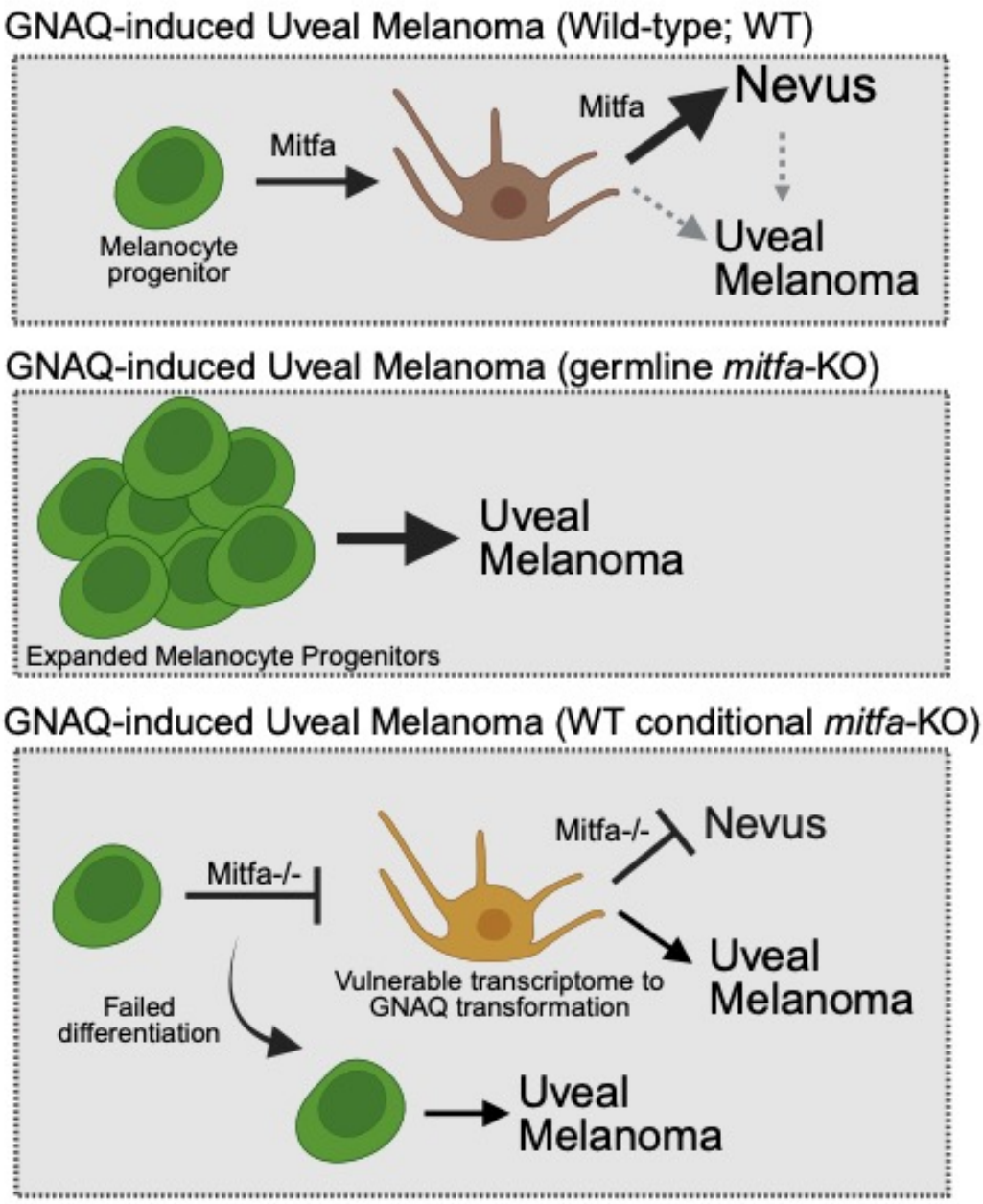

Graphical Abstract

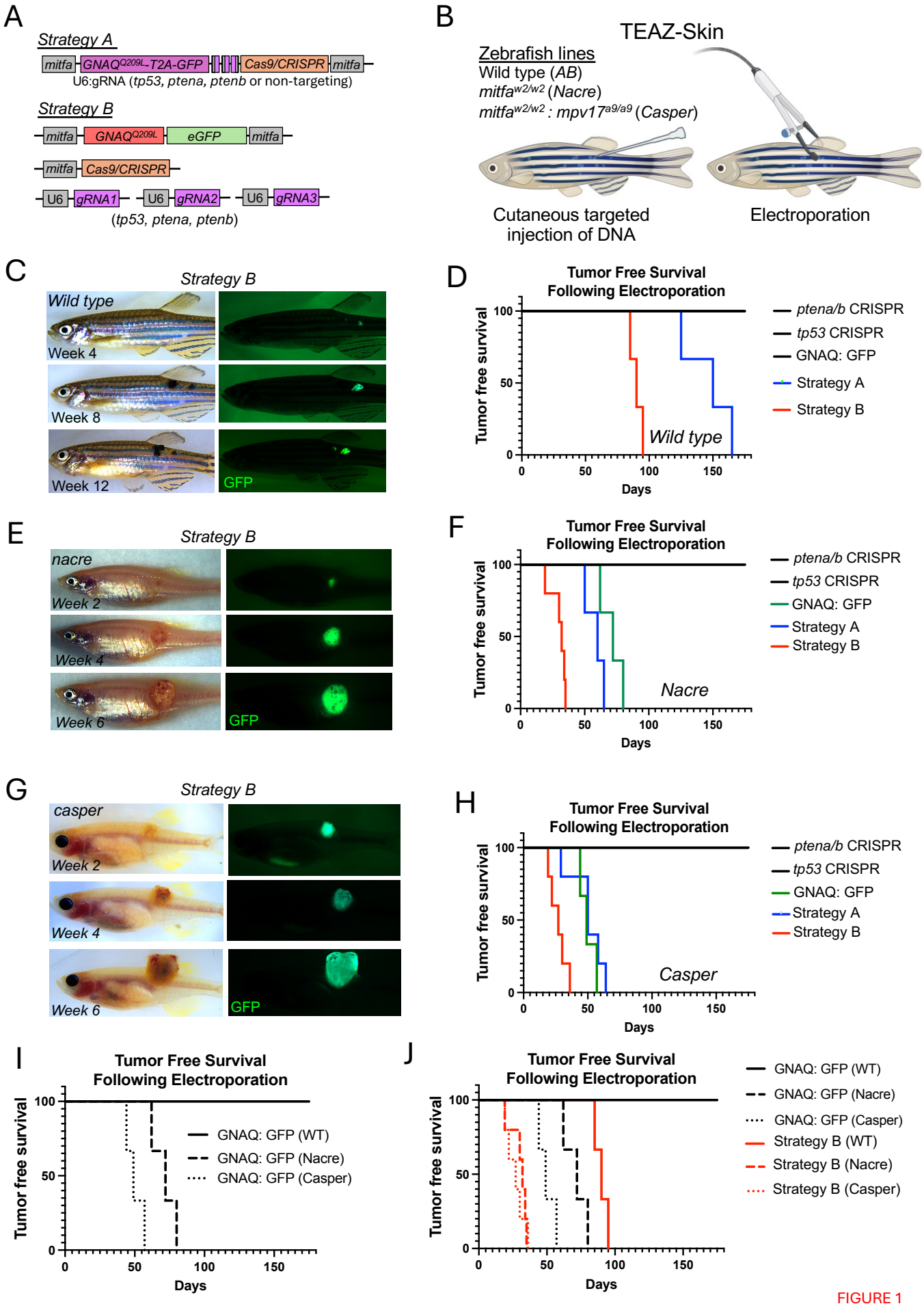
A
Strategy A
mitfa
GNAQQ209L-T2A-GFP
Cas9/CRISPR
mitfa
U6:gRNA (tp53, ptena, ptenb or non-targeting)
Strategy B
mitfa
GNAQQ209L
eGFP
mitfa
mitfa
Cas9/CRISPR
U6
gRNA1
U6
gRNA2
U6
gRNA3
(tp53, ptena, ptenb)
B
TEAZ-Skin
Zebrafish lines
Wild type (AB)
mitfaw2/w2 (Nacre)
mitfaw2/w2 : mpv17a9/a9 (Casper)
Cutaneous targeted injection of DNA
Electroporation
C
Strategy B
Wild type
Week 4
Week 8
Week 12
GFP
D
Tumor Free Survival Following Electroporation
Tumor free survival
Days
Wild type
ptena/b CRISPR
tp53 CRISPR
GNAQ: GFP
Strategy A
Strategy B
E
Strategy B
nacre
Week 2
Week 4
Week 6
GFP
F
Tumor Free Survival Following Electroporation
Tumor free survival
Days
Nacre
ptena/b CRISPR
tp53 CRISPR
GNAQ: GFP
Strategy A
Strategy B
G
Strategy B
casper
Week 2
Week 4
Week 6
GFP
H
Tumor Free Survival Following Electroporation
Tumor free survival
Days
Casper
ptena/b CRISPR
tp53 CRISPR
GNAQ: GFP
Strategy A
Strategy B
I
Tumor Free Survival Following Electroporation
Tumor free survival
Days
GNAQ: GFP (WT)
GNAQ: GFP (Nacre)
GNAQ: GFP (Casper)
J
Tumor Free Survival Following Electroporation
Tumor free survival
Days
GNAQ: GFP (WT)
GNAQ: GFP (Nacre)
GNAQ: GFP (Casper)
Strategy B (WT)
Strategy B (Nacre)
Strategy B (Casper)

FIGURE 1

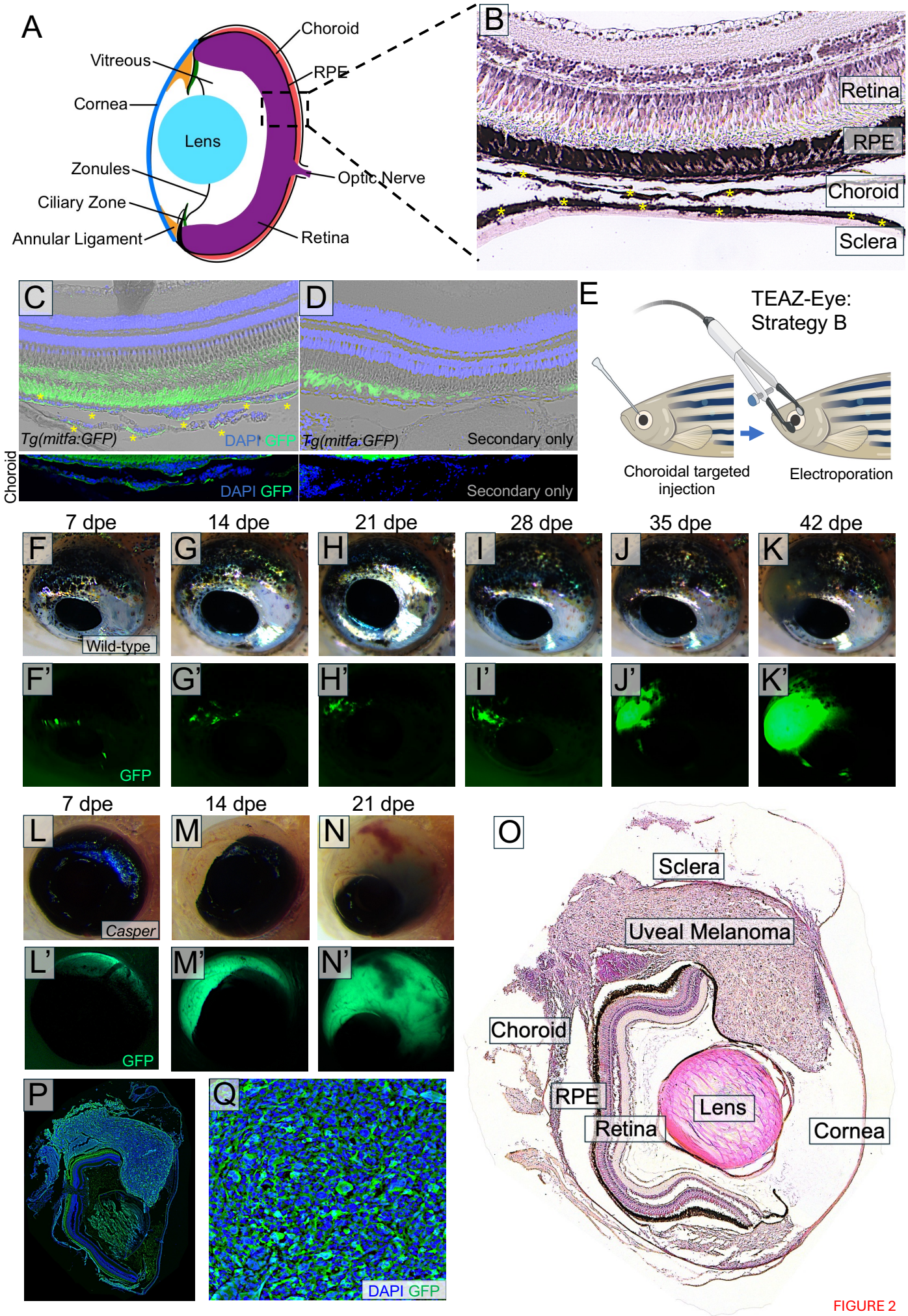
A
Choroid
Vitreous
RPE
Cornea
Lens
Zonules
Optic Nerve
Ciliary Zone
Annular Ligament
Retina
B
Retina
RPE
Choroid
Sclera
C
D
Tg(mitfa:GFP)
DAPI GFP
Tg(mitfa:GFP)
Secondary only
Choroid
DAPI GFP
Secondary only
E
TEAZ-Eye:
Strategy B
Choroidal targeted injection
Electroporation
7 dpe
14 dpe
21 dpe
28 dpe
35 dpe
42 dpe
F
G
H
I
J
K
Wild-type
F'
G'
H'
I'
J'
K'
GFP
7 dpe
14 dpe
21 dpe
L
M
N
Casper
L'
M'
N'
GFP
P
Q
DAPI GFP
O
Sclera
Uveal Melanoma
Choroid
RPE
Lens
Retina
Cornea

FIGURE 2

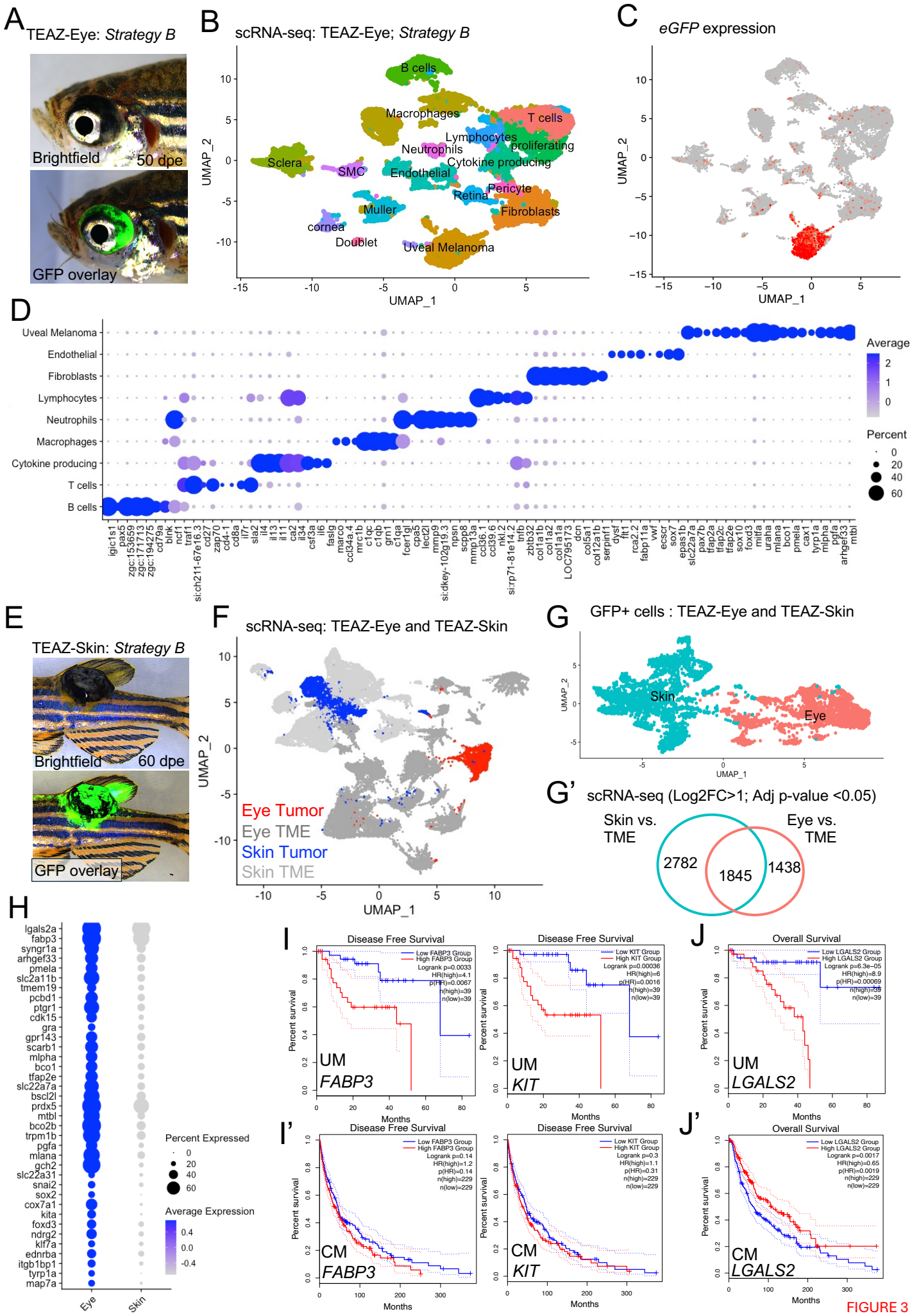
A
TEAZ-Eye: Strategy B
Brightfield
50 dpe
GFP overlay
B
scRNA-seq: TEAZ-Eye; Strategy B
B cells
Macrophages
T cells
Lymphocytes
proliferating
Neutrophils
Cytokine producing
Sclera
SMC
Endothelial
Pericyte
Retina
Muller
Fibroblasts
cornea
Doublet
Uveal Melanoma
UMAP_1
UMAP_2
C
eGFP expression
D
Uveal Melanoma
Endothelial
Fibroblasts
Lymphocytes
Neutrophils
Macrophages
Cytokine producing
T cells
B cells
Average
Percent
E
TEAZ-Skin: Strategy B
Brightfield
60 dpe
GFP overlay
F
scRNA-seq: TEAZ-Eye and TEAZ-Skin
Eye Tumor
Eye TME
Skin Tumor
Skin TME
G
GFP+ cells : TEAZ-Eye and TEAZ-Skin
Skin
Eye
G'
scRNA-seq (Log2FC>1; Adj p-value <0.05)
Skin vs. TME
Eye vs. TME
2782
1845
1438
H
Percent Expressed
Average Expression
Eye
Skin
I
Disease Free Survival
UM
FABP3
UM
KIT
J
Overall Survival
UM
LGALS2
I'
Disease Free Survival
CM
FABP3
CM
KIT
J'
Overall Survival
CM
LGALS2
Months
Percent survival

FIGURE 3

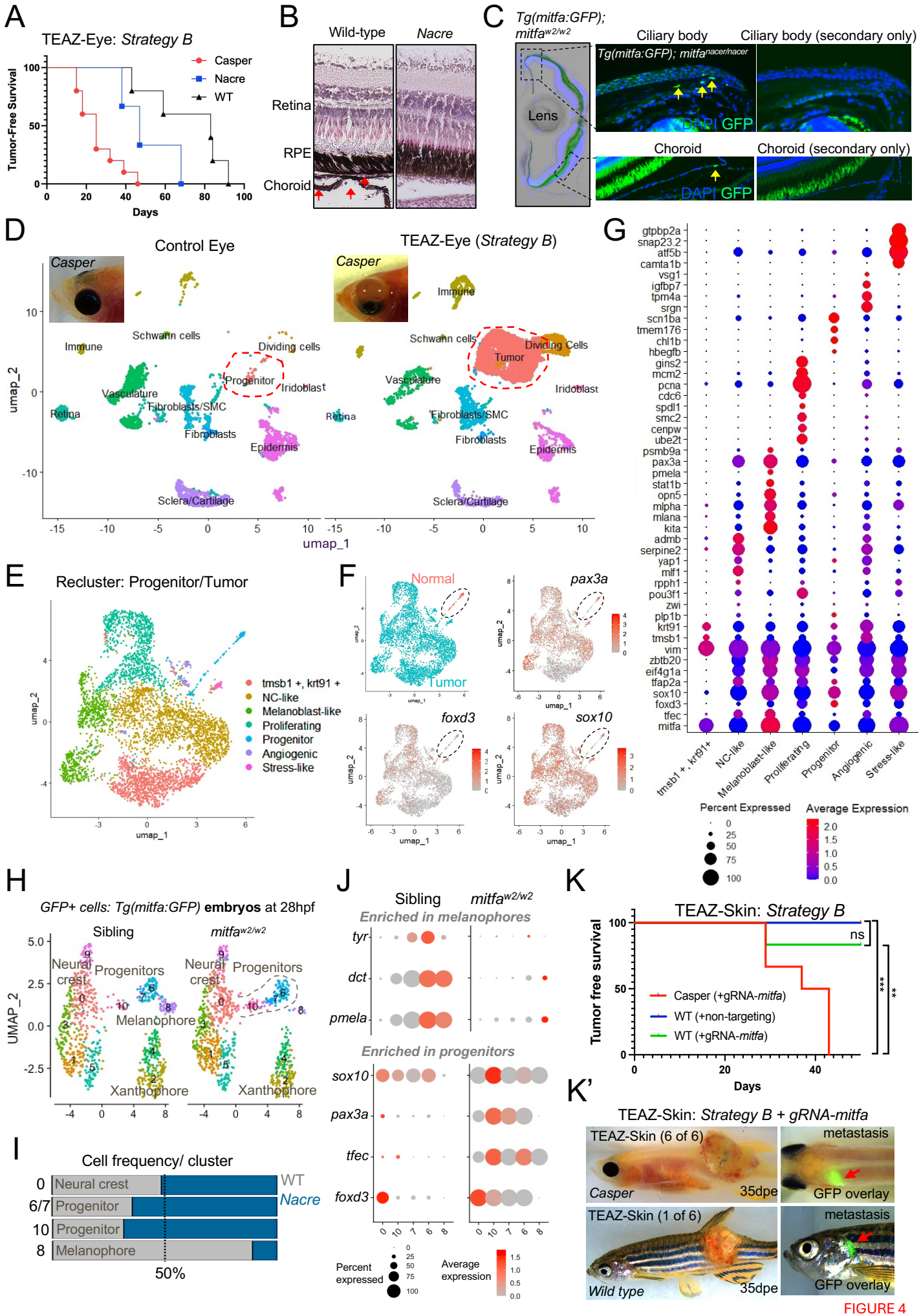
A
TEAZ-Eye: Strategy B
Casper
Nacre
WT
Tumor-Free Survival
Days
B
Wild-type
Nacre
Retina
RPE
Choroid
C
Tg(mitfa:GFP); mitfaw2/w2
Ciliary body
Ciliary body (secondary only)
Tg(mitfa:GFP); mitfanacer/nacer
Lens
DAPI GFP
Choroid
Choroid (secondary only)
D
Control Eye
TEAZ-Eye (Strategy B)
Casper
Immune
Schwann cells
Dividing cells
Tumor
Progenitor
Iridoblast
Vasculature
Fibroblasts/SMC
Fibroblasts
Retina
Epidermis
Sclera/Cartilage
umap_1
umap_2
E
Recluster: Progenitor/Tumor
tmsb1 +, krt91 +
NC-like
Melanoblast-like
Proliferating
Progenitor
Angiogenic
Stress-like
F
Normal
Tumor
pax3a
foxd3
sox10
G
tmsb1 +, krt91+
NC-like
Melanoblast-like
Proliferating
Progenitor
Angiogenic
Stress-like
Percent Expressed
Average Expression
H
GFP+ cells: Tg(mitfa:GFP) embryos at 28hpf
Sibling
mitfaw2/w2
Neural crest
Progenitors
Melanophore
Xanthophore
UMAP_2
I
Cell frequency/ cluster
WT
Nacre
Neural crest
Progenitor
Melanophore
50%
J
Sibling
mitfaw2/w2
Enriched in melanophores
tyr
dct
pmela
Enriched in progenitors
sox10
pax3a
tfec
foxd3
Percent expressed
Average expression
K
TEAZ-Skin: Strategy B
Tumor free survival
Days
ns
Casper (+gRNA-mitfa)
WT (+non-targeting)
WT (+gRNA-mitfa)
K'
TEAZ-Skin: Strategy B + gRNA-mitfa
TEAZ-Skin (6 of 6)
metastasis
Casper
35dpe
GFP overlay
TEAZ-Skin (1 of 6)
metastasis
Wild type
35dpe
GFP overlay

FIGURE 4

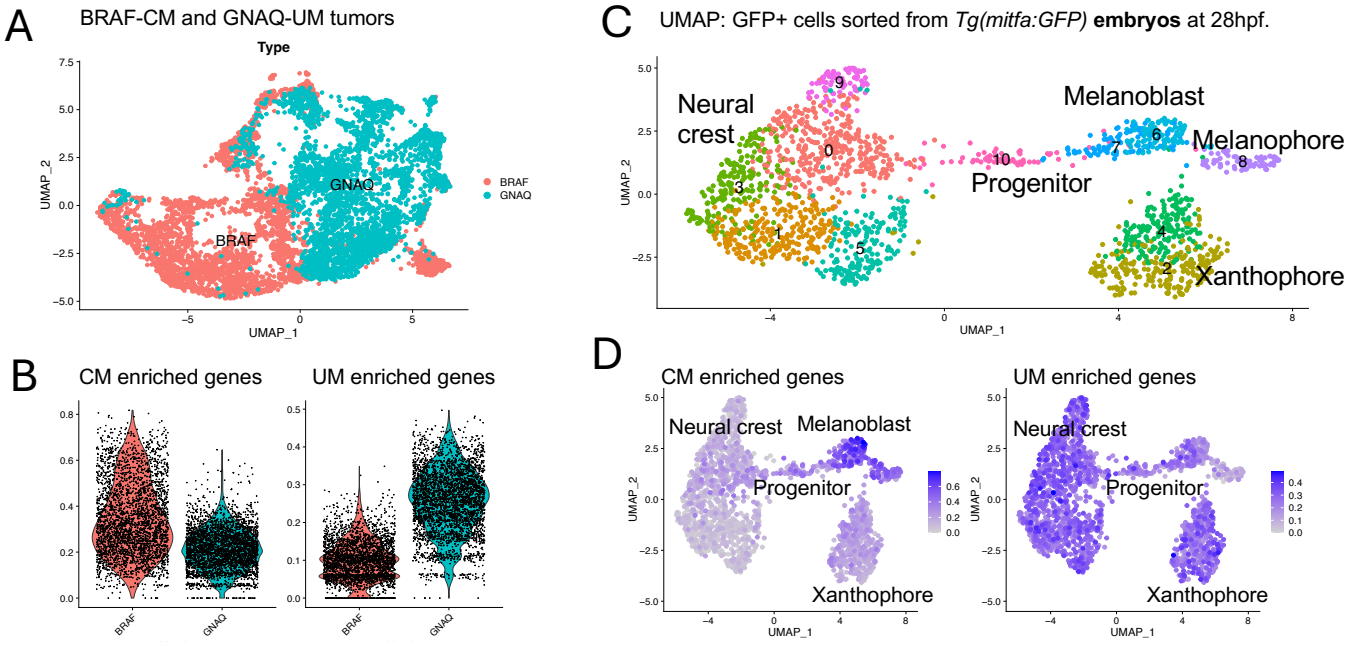
A
BRAF-CM and GNAQ-UM tumors
Type
BRAF
GNAQ
UMAP_1
UMAP_2
B
CM enriched genes
UM enriched genes
C
UMAP: GFP+ cells sorted from Tg(mitfa:GFP) embryos at 28hpf.
Neural crest
Melanoblast
Melanophore
Progenitor
Xanthophore
D
CM enriched genes
UM enriched genes
Neural crest
Melanoblast
Progenitor
Xanthophore

FIGURE 5